TÉCNICO LISBOA

# Numerical Simulation of Fire Whirls

**Rui Miguel Godinho Parente**

Thesis to obtain the Master of Science Degree in

## Mechanical Engineering

Supervisors: Prof. José Carlos Fernandes Pereira
Prof. José Manuel da Silva Chaves Ribeiro Pereira

### Examination Committee

Chairperson: Prof. Carlos Frederico Neves Bettencourt da Silva
Supervisor: Prof. José Manuel da Silva Chaves Ribeiro Pereira
Member of the Committee: Prof. Miguel Abreu de Almeida Mendes

**November 2018**

To my parents and sister

# Acknowledgments

I would like to thank to my supervisors Prof. José Chaves Pereira and Prof. José Carlos Pereira for all the guidance and disponibity. Without them it would not be possible to obtained the results discussed on this dissertation.

To my project colleagues Pedro Jorge and Pedro Marreiro for all the help through this dissertation.

To my LASEF colleagues, a big thank for the camaraderie, special to Duarte. To my friends Francisco, Manuel and Sofia for all the support during this work.

Finally I would like to thank to my parents for all the investment and support during the course. To my sister that although being a 8000 Km of distance, never stopped to support me.

# Resumo

Nesta dissertação é desenvolvida uma análise numérica de vórtice de fogo obtidos em condições laboratoriais. O modelo de turbulência Reynolds Stress Transport é empregue juntamente com o modelo de combustão Eddy Break-Up e com modelos de radiação. O vórtice de fogo 3D não estacionário é obtido recorrendo ao mesmo gerador de vórtice de fogo usado para trabalhos experimentais, consistindo em paredes com abertura forçando a entrada tangêncial de ar. A performance do modelo RST é comparada com observações experimentais e com modelos de duas equações RANS. É apresentada uma comparação detalhada entre previsões numéricas e observações experimentais, para uma gama de potências entre $2$ e $300$ kW. Os resultados estão de acordo com as observações experimentais e confirmam que o Burgers vórtice apresenta uma boa descrição da dinâmica do escoamento num vórtice de fogo. A dependência da altura de chama com a circulação foi deduzida recorrendo a leis de semelhança sendo validada com observações experimentais. Para cada potência considerada, foi encontrada uma circulação crítica que resulta na altura de chama máxima. Os campos turbulentos de vórtices de fogos são comparados com os campos de chamas sem rotação equivalentes, e são discutidos à luz do papel da supressão turbulenta e parâmetros de Richardson.

**Palavras-chave:** Vórtice de fogo, CFD, RST, Altura de chama, Circulação, Leis de semelhança

## Abstract

This dissertation presents a numerical study of laboratory fire whirls. The Reynolds Stress Transport model (RST) is used together with Eddy Break-Up combustion and radiation models. The unsteady 3D fire whirl prediction assume the same whirl generator used in laboratory consisting on enclosure walls to constrict airflow to enter tangentially in the facility. A low momentum fuel jet is located at the bottom centre of two halves of an offset hallow cylinder. The RST performance was compared with available experimental data and with two equations RANS turbulence models. A detailed comparison between available experimental data and numerical predictions, ranging from $2$ to $300$ kW are presented. The results are in good agreement with the available experimental data and confirm that the Burgers vortex gives a good description of the flow kinematics. The flame height dependence on circulation was deduced using scaling laws and validated with experimental data. For each heat release considered, a critical circulation was found that results in a maximum flame height. Fire whirl turbulence fields are compared with analogous non swirling flame and are discussed in light of the role of turbulent suppression and Richardson parameters.



**Keywords:** Fire whirls, CFD, RST, Flame height, Circulation, Scaling analysis

# Contents

# List of Tables

# List of Figures

# Nomenclature

### Greek symbols

| | |
|---|---|
| $\beta$ | Extinction coefficient |
| $\epsilon$ | Turbulence dissipation rate [$m^2/s^2$] |
| $\Gamma$ | Circulation [$m^2/s$] |
| $\kappa$ | Turbulent kinetic energy [$m^2/s^3$] |
| $\mu$ | Molecular viscosity [$Kg/ms$] |
| $\nu$ | Kinematic viscosity [$m^2/s$] |
| $\Omega$ | Angular velocity [$rad/s$] |
| $\omega$ | Vorticity [$s^-1$] |
| $\phi$ | Flux of vorticity [$m/s^2$] |
| $\rho$ | Density [$kg/m^3$] |
| $\tau$ | Viscous stress [$Pa$] |

### Roman symbols

| | |
|---|---|
| $\dot{m}$ | Fuel mass flow [$Kg/s$] |
| $D$ | Facility Diameter [$m$] |
| $g$ | Gravity accelation [$m/s^2$] |
| $H$ | Facility height [$m$] |
| $H_f$ | Flame height [$m$] |
| $R$ | Gas constant [$J/KgK$] |
| $R_i$ | Richardson number |
| $r_v$ | Vortex radius [$m$] |
| $Re$ | Reynolds number |

$T$ Temperature [$K$]

$U$ Velocity vector [$m/s$]

$Z$ Height [$m$]

$S$ Gap width [$m$]

**Subscripts**

$0$ With respect to burner.

$\lambda$ Wavelength $\lambda$.

$\theta, r, z$ Cylindrical components

$i, j, k$ Computational indexes

$t$ Turbulent

$x, y, z$ Cartesian components

**Superscripts**

$^*$ Non dimensional

# Glossary

**AIAA** American Institute of Aeronautics and Astronautics is a professional society for the field of aerospace engineering.

**CFD** Computational Fluid Dynamics is a field of fluid mechanics that solves numerically the govern equations.

**DNS** Direct Numerical Simulation is a simulation that solves the Navier-Stokes equation without any turbulence model.

**FDS** Fire Dynamics Simulation is a CFD code developed for solving fire driven flows.

**FVM** Finite Volume Method is a method for solving partial differential equations in algebraic form.

**LES** Large Eddy Simulation is a turbulence model for solving the Navier-Stokes equations ignoring the smallest turbulent length scales.

**LHV** Low Heating Value is the amount of heat release by combustion of a certain fuel which assumes the latent heat of vaporization of water in the reaction products is not recovered.

**RANS** Reynolds Average Numerical Simulation is a turbulence model that solves the Navier-Stokes equations in average.

**RST** Reynolds Stress Transport is a turbulence model where the Reynolds stress tensor is directed computed.

**SIMPLE** Semi Implicit Method for Pressure Linked Equations is a numerical procedure to solve the Navier-Stokes equations.

# Chapter 1

# Introduction

## 1.1 Motivation

Fire whirls are dangerous flame structures that arise from the interaction of buoyant flames and ambient vorticity. They may appear on forest and urban fires. They are associated with strong buoyant fire motion, originating an increase in burning rates and large radiative heat fluxes compared with normal fires. The vertical flows are capable of lifting and toss burning debris over large distances, making difficult fire extinction. In addition their unexpected occurrence and behaviour are associated with fire spread intensification and difficulties in fire extinction, representing great danger specially for firefighters and also for inhabitants as remembered on the historical Tokyo disaster, where $38000$ people were killed [1] and the Chicago fire in 1971 responsible for $300$ fatalities [2].
Fire whirls are still a relatively poorly understood phenomenon, and several scenarios have been put forward for their occurrence but without a definitive proof. Among the conditions in wildland that have been identified as more likely potential ones are: multiple flames channelling tangential air entrainment, L-shape obstacles and other structures, recirculating vortices on the lee side of hills, etc. see figure 1.1. Recently it is believed that fire whirls may be driven by counter rotating vortex pair of the plume of the flame. This result suggests that in large fires, the flamewake is a possible origin of the fire whirls that occur downwind of a fire area and are shed downwind.

Despite sharing some characteristics with an atmospheric tornado, the formation condition and sources of fire whirls differs greatly from tornado. Basically, the tornado is originated in the upper atmospheric layers while fire whirls are originated on the ground. In order to occur, fire whirls require three major mechanisms [3]:

- A heat source responsible for create a buoyancy force;
- A vorticity generation mechanism in order to create a rotational field;
- Surface drag force to create a radial boundary layer that facilitates the air and vorticity entrainment into the vortex.

The complexity associated to the fire whirl phenomenon is well illustrated with the existence of 13 non

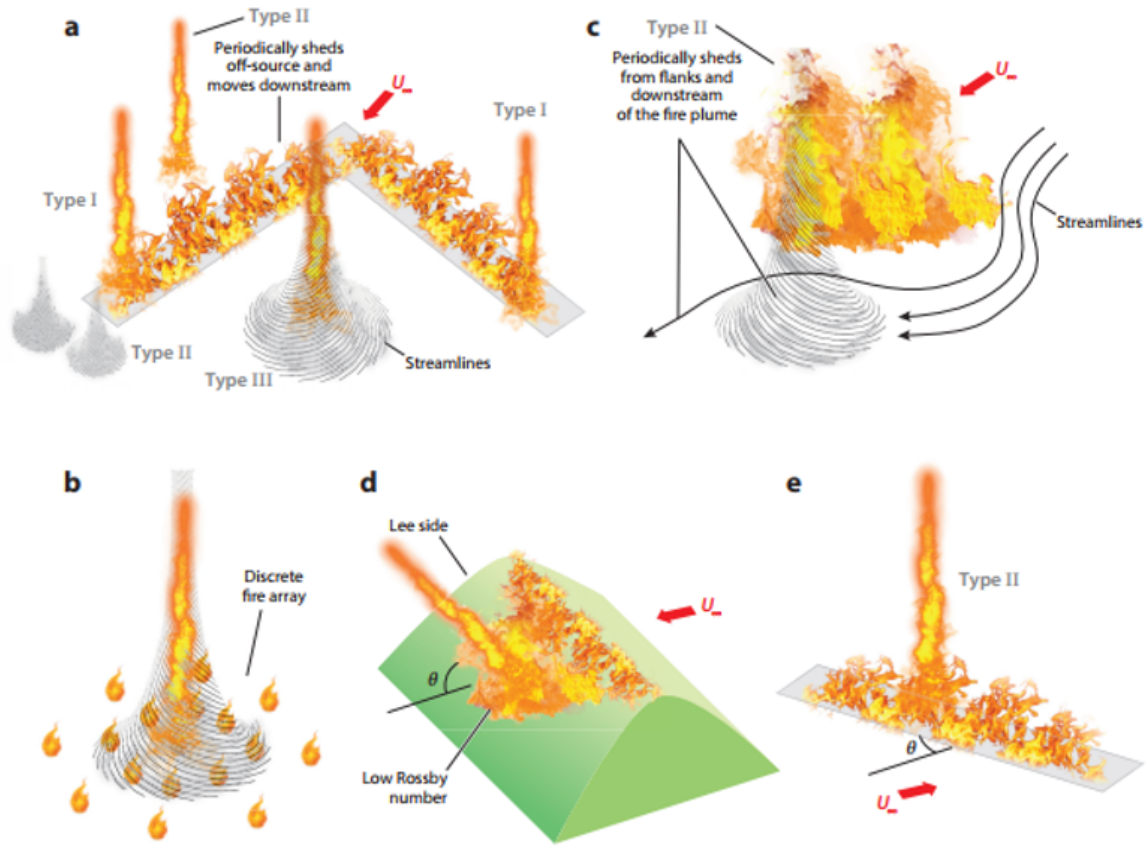


Figure 1.1: Several open configurations favourable for the formation of fire whirls. Source [3]

dimensional groups [3]. Among these 13 non dimensional groups, important and well know parameters, such as Froude number (Fr), Reynolds number (Re), Prandtl number (Pr), Rossby number (Ro), Grashof number (Gr) and the Richardson and Rayleigh numbers (Ri and Ra) are present. The non dimensional groups are very important to investigate numerically or experimentally the similitude characteristics of fire whirls. Unfortunately, the number of permutations required to investigate the influence of 13 non-dimensional parameters groups is prohibitive. Although some authors have focussed their description on a few of 2 or 3 non dimensional parameters such as flame height and mass flow as function of circulation [4, 5, 6, 7, 8], the fundamental knowledge of the driving mechanism and physical behaviour is still not fully understood.

The increase of flame height observed in fire whirls compared with analogous non swirling flames is presented not only on pool fires where the fuel consumption increases but also on burners with constant heat releases.

Despite of fire whirls being associated with natural disasters and negative social and economic impact, recent studies [9, 10] discover a new combustion state of fire whirl, which it is called ”blue whirls”. It was found that it presents a cleaner combustion process than conventional combustion and fire whirls. The growing worldwide demand to reduce emissions from combustion calls for the development of alternative technologies of high-efficiency and low-emissions combustion. The new state ”blue whirl” presents an important step forward on combustion technology but firstly the fire whirl phenomenon needs to be fully

understood.

Due to the increase in computational power, numerical simulations have become a viable tool for studies of complex phenomenons such as fire whirls. The availability of information and details delivered by numerical simulations represent a great addition on better understand of fire whirls on several levels and different scenarios.

## 1.2 Literature Review

### 1.2.1 Experimental Work

The experimental study of fire whirls is usually carried out adopting two kind of heat sources, either a fixed heat release such as low momentum burners [4, 11] or solid fuels [12] and pool burning [8, 13]. The fire whirl geometrical configurations are designed to promote the required entrainment with tangential momentum.

Usually they consist of an enclosure facility with rotating side walls or fixed walls with slits to promote tangential entrainment. A few others mechanisms are used such as obstacles that generate vortical structures [5, 7] or fire merging and multiple flames [14, 15, 16]. The different types of enclosure facilities have been reviewed by Tohidi *et al.* [3]. The influence of the entrainment gap width on the flame

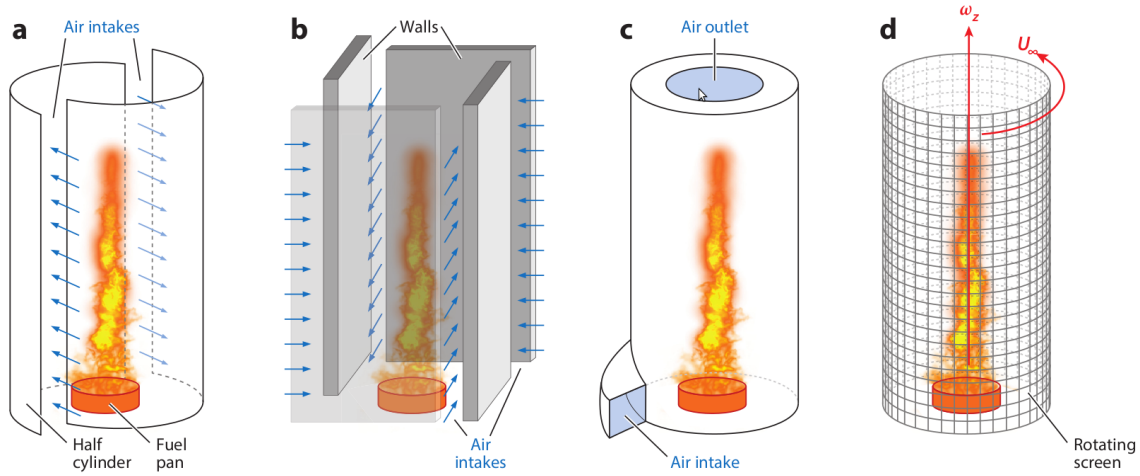


Figure 1.2: Four types of experimental enclosure facilities (a) staggered cylinders, (b) square section with four entries, (c) circular intake, (d) self-rotating screen know as Emmons facility. Source [3]

height and stability of fire whirls was investigated by Yu *et al.* [17] using a fixed frame facility, which concluded that for small gap widths no fire whirl was observed. Battaglia *et al.* [18] and Zhou and Wu [16] reported that low circulation values have a negative impact on the flame height. Hartl and Smits [4] and Forthofer and Goodrick [2] reported that flame height increases with circulation. Snegirev *et al.* [19] observed that the flame height increase with circulation, reaching the highest value when the swirl number was equal to 0.6. Lei *et al.* [20] concluded that the circulation for which the flame height is maximum depends on the heat release. Further increase in circulation will result in a decrease on the

flame height. Finally, for extreme high circulation values vortex breakdown may occur decreasing the flame height, see e.g Tohidi *et al.* [3] Zhou *et al.* [21] and Lei *et al.* [20].
Lei *et al.* [22] studied the fire whirls flame height in light of the role of turbulent suppression and Richardson parameters.
Chow and Han [23] compared the difference between fire whirls generated from different heat source either with fixed fuel rate supply or solid and liquid fuels with a swirling plume. Lei *et al.* and Lei and Liu [24, 25, 26] studied the effect of circulation on formation and stability of small heat release fire whirls. Dobashi *et al.* [1] observed that fire whirl has large radiant fluxes than analogous non swirling buoyant flame and that the presence of a Ekman type boundary layer modified the base shape of a fire whirl generated from liquid fuels. Finally, Wang *et al.* [27] tested the effect of replace solid walls by air curtains on a fire whirl generator. A stable fire whirl is obtained, however it is necessary to tilt outward the air curtain generator, in order to no interact with the fire whirl generate inside of the facility.
Although the challenges imposed by the complexity of the fire whirl behaviour, some researchers have put some effort into the theoretical analysis of fire whirls. Their studies have mainly focused on increase of flame height. Yu and Zhang [28, 29, 30] and Klimenko and Willims [31] studied the increase the flame height in light of Peclet number. Although their conclusions follow the experimental and numerical observations in a qualitative way, several simplifications such as constant density, lack of radiation and combustion chemistry effect, were employed in such studies.

### 1.2.2 Numerical Studies

The complexity of the phenomenon also create modelling difficulties and very few numerical studies have been validated against experimental data. Battaglia *et al.* [18] reported one of the first attempts in numerical modelling of fire whirls simulation using FDS computer code with Large Eddy Simulation in order to recreate the pioneer experimental work of Emmons and Ying [32]. Others FDS simulation studies have followed like Yuen *et al.* [33] which recreated the experimental work of Chow *et al.* [23] but the temperature field was over predicted while Zou *et al.* [34] reported reasonable agreement with the measured flame height and centre line temperature profiles.
The few reported simulations do not include validation of the turbulent field of the fire whirl. It is well know the lack of performance of two equation turbulence models as $\kappa - \epsilon$ to simulate flows dominated by buoyancy and swirl, see e.g Hanjalic [35] and Pereira and Rocha [36, 37]. Several models extension of the standard $\kappa - \epsilon$ have been proposed. Chow *et al.* [23, 38] used the RNG $\kappa - \epsilon$ from the commercial code FLUENT to validate the assumption of a Burgers vortex flow behaviour on the fire whirl core but only the flame height was compared with the experimental work. Other two equation turbulence models variants were compared, see e.g Snegirev *et al.* [19] but second order closures offer better prospects than eddy viscosity models for capturing at least some of the complex phenomenon of buoyant turbulent flows. Consequently, numerical simulation of fire whirls constitute a great challenge due to the modelling but also the computational power required if LES modelling is selected.

## 1.3 Objectives

The primary objective of this dissertation is to investigate the effect of circulation on fire whirl structure. In order to fulfil this purpose, the 3D unsteady simulations are validated against several fire whirls experiments ranging from $2$ to $300$ kW. The role of the boundary layer on the fire whirl base shape is studied. Finally, the role of turbulence suppression on the flame height elongation of turbulent fire whirls is investigated.

## 1.4 Thesis Outline

This dissertation is organized as follows: in chapter 2 the fundamentals of fluid mechanics are discussed as well as the mathematical models used in order to fulfil the purposed objectives. In chapter 3 the numerical implementation are developed. Special attention is given to the simulation validation against experimental work, since it is one of the main objectives. In chapter 4 the role of circulation on the fire whirl structure is discussed. A correlation of flame height as function of circulation is developed and validated with experimental data. Finally, the last chapter is dedicated to main conclusions and proposals for future work.

# Chapter 2

# Fundamentals

Before proceeding for the results and methodology, a short review of the governing equations is made. Subsequently, the numerical models used are presented, in particular the turbulence, combustion and radiation models. Finally, the non-dimensionally quantities of interest are presented.

## 2.1 Governing Equations

The governing equations that rule the flow behaviour are based on the following conservation laws:

- Conservation of mass;
- Newton's second law (conservation of momentum);
- First law of thermodynamics (conservation of energy);

Conservation of mass states that for a control volume there is no generation or depletion of mass, so mass is conserved within the control volume. For an infinitesimal control volume is defined as follows [39]:

$$\frac{\partial \rho}{\partial t} + \frac{\partial (\rho u_i)}{\partial x_i} = S_m \tag{2.1}$$

As mentioned before the conservation of momentum is based on the Newton's second law. For an infinitesimal volume it is defined as follows [40]:

$$\begin{aligned}
\rho g_x - \frac{\partial p}{\partial x} + \frac{\partial \tau_{xx}}{\partial x} + \frac{\partial \tau_{yx}}{\partial y} + \frac{\partial \tau_{zx}}{\partial z} &= \rho \left( \frac{\partial u}{\partial t} + u\frac{\partial u}{\partial x} + v\frac{\partial u}{\partial y} + w\frac{\partial u}{\partial z} \right) \\
\rho g_y - \frac{\partial p}{\partial y} + \frac{\partial \tau_{xy}}{\partial x} + \frac{\partial \tau_{yy}}{\partial y} + \frac{\partial \tau_{zy}}{\partial z} &= \rho \left( \frac{\partial v}{\partial t} + u\frac{\partial v}{\partial x} + v\frac{\partial v}{\partial y} + w\frac{\partial v}{\partial z} \right) \\
\rho g_z - \frac{\partial p}{\partial z} + \frac{\partial \tau_{xz}}{\partial x} + \frac{\partial \tau_{yz}}{\partial y} + \frac{\partial \tau_{zz}}{\partial z} &= \rho \left( \frac{\partial w}{\partial t} + u\frac{\partial w}{\partial x} + v\frac{\partial w}{\partial y} + w\frac{\partial w}{\partial z} \right)
\end{aligned} \tag{2.2}$$

In a Newtonian fluid the viscous stresses $\tau$ are modelled as follows [40]:

$$
\begin{aligned}
\tau_{xx} &= 2\mu\frac{\partial u}{\partial x} + \lambda\nabla U \\
\tau_{yy} &= 2\mu\frac{\partial v}{\partial y} + \lambda\nabla U \\
\tau_{zz} &= 2\mu\frac{\partial w}{\partial z} + \lambda\nabla U \\
\tau_{xy} &= \tau_y x = \mu(\frac{\partial u}{\partial y} + \frac{\partial v}{\partial x}) \\
\tau_{xz} &= \tau_z x = \mu(\frac{\partial u}{\partial z} + \frac{\partial w}{\partial x}) \\
\tau_{yz} &= \tau_z y = \mu(\frac{\partial w}{\partial y} + \frac{\partial v}{\partial z})
\end{aligned} \tag{2.3}
$$

The substitution of equation (2.3) on the equation of conservation of momentum (2.2) yields to the so called Navier-Stokes Equations for a flow with constant density and viscosity:

$$
\begin{aligned}
\rho g_x - \frac{\partial p}{\partial x} + \mu\left(\frac{\partial^2 u}{\partial x^2} + \frac{\partial^2 u}{\partial y^2} + \frac{\partial^2 u}{\partial z^2}\right) &= \rho\frac{du}{dt} \\
\rho g_y - \frac{\partial p}{\partial y} + \mu\left(\frac{\partial^2 v}{\partial x^2} + \frac{\partial^2 v}{\partial y^2} + \frac{\partial^2 v}{\partial z^2}\right) &= \rho\frac{dv}{dt} \\
\rho g_z - \frac{\partial p}{\partial z} + \mu\left(\frac{\partial^2 w}{\partial x^2} + \frac{\partial^2 w}{\partial y^2} + \frac{\partial^2 w}{\partial z^2}\right) &= \rho\frac{dw}{dt}
\end{aligned} \tag{2.4}
$$

For generic flows (variable density, viscosity, etc.) the Navier-Stokes equations for momentum read as:

$$
\frac{\partial \rho U}{\partial t} + \nabla\cdot(U\otimes U) = -\nabla P + \nabla\cdot\tau + \rho g \tag{2.5}
$$

The conservation of energy is expressed by the energy equation:

$$
\frac{\partial \rho h_t}{\partial t} + \nabla\cdot(\rho h_t U) = \nabla\cdot(\tau\cdot U) - \nabla\cdot(\kappa\nabla T) + \frac{\partial p}{\partial t} + f_b\cdot U + q_v \tag{2.6}
$$

where $\kappa$ is the thermal conductivity and $h_t$ is the total enthalpy and is expressed as follows:

$$
h_t = c_p T + \frac{1}{2}u^2 \tag{2.7}
$$

In order to compute the relation between key properties such as temperature, pressure and density, a equation of state is needed. Through out this dissertation it was assume that the fluid can be modelled as an ideal gas, leading to the following equation of state:

$$
p = \rho R T \tag{2.8}
$$

## 2.2 Rotating Flows

### 2.2.1 Basic aspects of vorticity

According to Batchelor(1967), for cylindrical coordinates $(r, \theta, z)$ the flow rotation is characterised by the following kinematic quantities:

$$\vec{\omega} = \nabla \times \vec{U} = \left( \frac{1}{r}\frac{\partial u_z}{\partial \theta} - \frac{\partial u_\theta}{\partial z}, \frac{\partial u_r}{\partial z} - \frac{\partial u_z}{\partial r}, \frac{1}{r}\left( \frac{\partial r u_\theta}{\partial r} - \frac{\partial u_r}{\partial \theta} \right) \right) \tag{2.9}$$

where $u_r, u_\theta, u_z$ are the radial, angular (tangential) and axial velocity components.
The previous equation leads to the conclusion that vorticity ($\omega$) is twice the value of the angular velocity of the fluid particle [41]:

$$\Omega = \frac{v_\theta}{r} = \frac{\omega}{2} \tag{2.10}$$

where $\Omega$ is the angular velocity.
Considering a two dimensional flow and that the element of fluid is circular with a radius r and bounded through curve c, the application of Stokes theorem leads to the following result:

$$\omega \pi r^2 = \oint_c u \cdot \partial l \tag{2.11}$$

The flux of vorticity $\phi$ is constant through any surface leading to the Kelvin's theorem:

$$\Gamma = \oint_c u \cdot \partial l = constant \tag{2.12}$$

where $\Gamma$ is called circulation. The application of Kelvin's theorem to a vortex tube, see figure 2.1, leads to the conclusion that circulation can be computed from the surface integral of vorticity.

$$\phi = \int \omega \cdot \partial s = \oint_c u \cdot \partial l = \Gamma \tag{2.13}$$

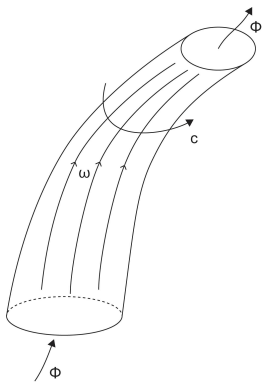


Figure 2.1: Example of a vortex tube

### 2.2.2 Vorticity Equation

Examining the definition of the vorticity vector (2.9), using the Navier Stokes equation, we can derived the vorticity equation that govern the evolution of vorticity in the flow:

$$\frac{D\vec{\omega}}{Dt} = \underbrace{(\vec{\omega}\cdot\nabla)\,\vec{U}}_{\text{Vortex tube stretching}} - \underbrace{\vec{\omega}\left(\nabla\cdot\vec{U}\right)}_{\text{Vortex tube tilting}} + \underbrace{\frac{\nabla\rho\times\nabla P}{\rho^2}}_{\text{Baroclinic production of vorticity}} + \underbrace{\nabla\times\vec{F}_f}_{\text{Body forces}} \tag{2.14}$$

1. The left side of the equation represents the transport of vorticity throughout the domain.
2. The vortex tube stretching term represents the straining effect on the fluid elements duo to stretching, which can produce or dissipate vorticity.
3. The vortex tube tilting term represents the transfer of vorticity between the different Cartesian components.
4. The baroclininc term represents the vorticity production duo to the misalignment of pressure and density gradients.
5. The body forces term represents the variations on the vorticity field due to external forces.

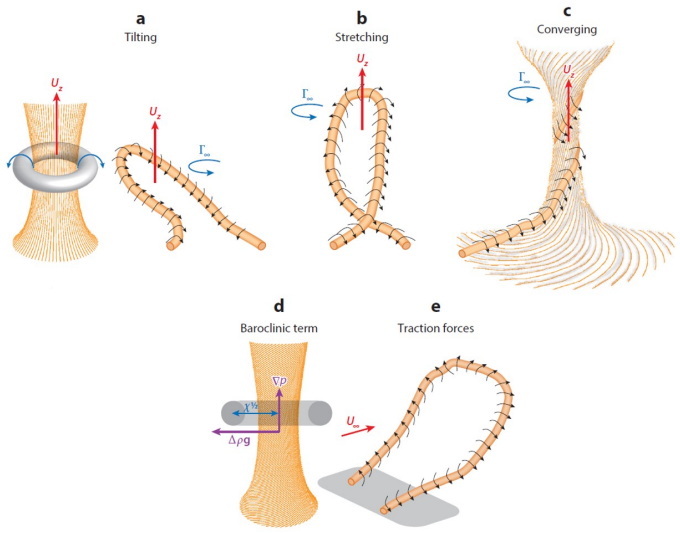


Figure 2.2: Schematics of the vorticity equation terms. Source [3]

### 2.2.3 Vortex Structure

Assuming a bi-dimensional flow and that the trajectories are circulars, from equation 2.9:

$$\Omega_z = \frac{1}{r}\frac{\partial}{\partial r}\left(r u_\theta\right) \tag{2.15}$$

the condition of irrotationality implies that $ru_\theta = constant$. The condition $ru_\theta = constant$ applied to the equation 2.13 implies the following:

$$u_\theta = \frac{\Gamma}{2\pi r} \tag{2.16}$$

A flow with this characteristic is called a *free vortex* [42].
On the centre of a vortex a core with solid rotation must exist. The radial evolution of tangential velocity on the core must be $\frac{u_\theta}{r} = constant = \Omega$. This implies:

$$\Gamma_z = \frac{1}{r}\frac{\partial}{\partial r}\left(ry_\theta\right) = \frac{1}{r}\frac{\partial}{\partial r}\left(\Omega r^2 = 2\Omega\right) \tag{2.17}$$

A vortex with this characteristic is called *forced vortex*.
This two kind of vortices cannot exist alone. For instance, in the case of a *forced vortex*, the influence of a perturbation is proportional to the distance leading to an unphysical situation. On the other hand the presence of circulation requires a core with vorticity which is incompatible with the definition of *free vortex*. Therefore a ”real vortex” (*combined vortex*) results of a combination of a *free vortex* and a *forced vortex*. For a core radius of r=a, the combined vortex as the following properties [42]:

$$\text{Core} \qquad \frac{r}{a} \leq 1 \qquad\qquad \text{Outer region} \qquad \frac{r}{a} > 1$$

$$u_\theta = \Omega r \qquad\qquad u_\theta = \frac{\Gamma}{2\pi r}$$

$$\omega = \frac{\Gamma}{\pi a^2} = constant \tag{2.18} \qquad\qquad \omega = 0 \tag{2.19}$$

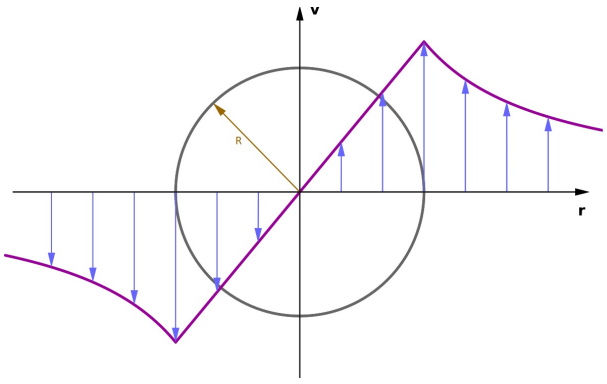


Figure 2.3: Tangential velocity distribution on a ”real vortex”

## 2.3 Numerical Methods

### 2.3.1 Turbulence Modelling

As previous mentioned, turbulence plays an important role on predicting fire whirls. According to Hinze [43] *”Turbulent fluid motion is an irregular condition of flow in which the various quantities show a random*

*variation with time and space coordinates, so that statistically distinct average values can be discerned."*
In fact turbulence is characterized by rapid velocity and pressure fluctuations leading to an unsteady and chaotic fluid motion. Such behaviour represents a great numerical challenge in order to satisfactory predict the fluid motion.
There are mainly three approaches to numerically solve the turbulence problem. It can be directed solve, by solving without any additional model the fluid motion equations. It can be solved only for the scales of interest, using filtered quantities (LES), or by solving the fluid motion in time average.
The prohibitive computational cost of solving directly the governing equations (DNS) and the considerable cost of using the LES approach dictates the selection of Reynolds-Average Navier-Stokes (RANS).
On the Unsteady Reynolds Averaged Navier-Stokes (URANS) turbulence, a generic variable $\phi$ (velocity, pressure etc) in the instantaneous Navier-Stokes equations is decomposed in its average value plus the fluctuation:

$$\phi(x,t) = \lim_{N\to\infty} \frac{1}{N} \sum_{k=1}^{N} \phi_k(x,t) \tag{2.20}$$

The time averaged form of the compressible Navier-Stokes equation for the continuity, momentum and energy equation reads as:

$$\begin{aligned} \frac{\partial \rho}{\partial t} + \nabla \cdot \left[\rho \bar{U}\right] &= 0 \\ \frac{\partial}{\partial t}\left(\rho \bar{U}\right) + \nabla \cdot \left[\rho \bar{U}\bar{U}\right] &= -\nabla \cdot pI + \nabla \cdot (T + T_t) + f_b \\ \frac{\partial}{\partial t}\left(\rho E\right) - \nabla \cdot \left(U\left(\rho E - P\right)\right) &= \nabla \cdot \left[\left(K + \frac{C_p \mu_t}{Pr_t}\right) \nabla \cdot TU(T_f)\right] + S_h \end{aligned} \tag{2.21}$$

where $I$ is the identity tensor, $T$ is the viscous stress tensor, $T_t$ the Reynolds stress tensor, $T_f$ the turbulent heat flux vector and $f_b$ is the resultant of the body forces (such as gravity and centrifugal forces).
The time average Navier-Stokes and energy equations were close by RST, where all components of the Reynolds Stress Tensor are directly computed by transport equation. In the RST model the transport equation for the specific Reynolds stress tensor $R = \frac{-T_f}{\rho}$ is defined as follows:

$$\frac{\partial}{\partial t}\left(\rho R\right) + \nabla \cdot \left(\rho R \bar{U}\right) = \nabla \cdot D + P + G - \frac{2}{3}\rho I \gamma_M + \underline{\phi} + \underline{\epsilon} + S_r \tag{2.22}$$

where $\gamma_M$ is the Dilatation Dissipation, $\underline{\epsilon}$ is the turbulent dissipation rate tensor and $S_R$ is a specified source. The generalized gradient diffusion ($D$) was used for the turbulent heat flux vector.
The selection of RST model to close the time average Navier-Stokes and energy equations is discussed in detail on the following chapter.

### 2.3.2 Combustion and Radiation

The Eddy Break Up (EBU) model from Spalding [44] and Magnussen and Hjertager [45] was selected. The individual species are transported at different rates according to their own governing equations. The time average of the instantaneous governing equations can be written as follows:

$$\frac{\partial}{\partial t}\left(\rho\chi\bar{Y}_i\right) + \nabla\cdot\left(\rho U\bar{Y}_i - \bar{F}_i\right) = \bar{S}_i \tag{2.23}$$

where $F_i$ is the diffusion flux and is defined as:

$$F_i = \left(D_i + \frac{\mu_t}{Sc_i}\right)\nabla\bar{Y}_i \tag{2.24}$$

The mixing controlled rate of reaction is expressed in terms of the turbulence time scale $\frac{\kappa}{\epsilon}$. The individual dissipation rates for fuel, oxygen and combustion products are expressed as follows:

$$\dot{w}_{fu} = C_r\bar{\rho}Y_{fu}\frac{\epsilon}{\kappa} \tag{2.25}$$

$$\dot{w}_{ox} = C_r\bar{\rho}\frac{Y_{ox}}{s}\frac{\epsilon}{\kappa} \tag{2.26}$$

$$\dot{w}_{pr} = C_r\bar{\rho}\frac{Y_{pr}}{1+s}\frac{\epsilon}{\kappa} \tag{2.27}$$

where $Y$ is the component mass and $s$ is the stoichiometric coefficient. For the actual reaction rate of fuel, the Eddy Break-Up takes in account the individual dissipation rates and assumes that it is equal to the slowest one:

$$R_f = -\rho\frac{\epsilon}{\kappa}min\left[C_rY_{fu}, C_r\frac{Y_{ox}}{s}, C_r\frac{Y_{pr}}{1+s}\right] \tag{2.28}$$

Radiation plays an important role on fire whirls. Duo to the increase of height and change of the shape, comparing with ordinary diffusion flames, the radiative flux change from ordinary diffusion flames to fire whirls. Furthermore, without radiation modelling a considerable error was made on the prediction on the flame front and plume temperature, since it can be considerable higher without radiation modelling.
As radiation travels through a participating media, the material that is present in the media can absorb, emit, or scatter radiation. The effect on the radiant intensity is govern by the following equation:

$$\frac{\partial I_\lambda}{\partial s} = -\beta_\lambda I_\lambda + \kappa_{a\lambda}I_{b\lambda} + \frac{\kappa_{s\lambda}}{4\pi}\int_{4\pi} I_\lambda(\Omega)\partial(\Omega) + \kappa_{pa\lambda}I_{pb\lambda} + \frac{\kappa_{ps\lambda}}{4\pi}\int_{4\pi} I_\lambda(\Omega)\partial(\Omega) \tag{2.29}$$

The field equation for radiation intensity is solved with the Discrete Ordinates Method (DOM):

$$s_i\cdot\nabla I_{i\delta\lambda} = -\beta_{\delta\lambda}I_{i\delta\lambda} + \kappa_{a\delta\lambda}I_{b\delta\lambda} + \frac{\kappa_{s\delta\lambda}}{4\pi}\sum_{j=1}^{n} w_jI_{j\delta\lambda} + \kappa_{\bar{p}\delta\lambda}I_{p\delta\lambda} + \frac{\kappa_{\bar{p}\delta\lambda}}{4\pi}\sum_{j=1}^{n} w_jI_{j\delta\lambda} \tag{2.30}$$

where $\kappa_a$ is the absorption coefficient, $\kappa_s$ is the scattering coefficient, $\kappa_{po}$ is the particle absorption and $I_b$ is the black body intensity.

Finally the absorption coefficient is calculated with the Weighted Sum of Gray Gases (WSGG). This method makes use of the Hottel charts and sum-of-gray-gases models for a mixture containing $CO_2$ and/or $H_2O$ gases only. The total absorptivity is computed as follow:

$$a \approx \sum_{\kappa=0}^{\kappa} a_\kappa \left(1 - e^{-K_\kappa S}\right) \tag{2.31}$$

where $K$ is the total number of gray gases, $a_\kappa$ is the weight factor, $K_\kappa$ is the absorption coefficient of each gray gas and $S$ is the optical thickness.

## 2.4 Non dimensional analysis

The dangerous nature of fire whirls increases the difficulties on the studies of the phenomenon. Therefore dimensional analysis plays an important role on the better understanding of fire whirls. According to [3], the influential parameters are:

$$(u_r, u_z, \Gamma, H, \dot{m}) = \phi(L_h, \dot{Q}, C_p, \Delta\rho, \rho, \Delta T, T, g, \mu, \beta, \kappa, D_s) \tag{2.32}$$

where $u_r$ and $u_z$ are the radial and axial velocities, respectively. H is the flame height. $L_h$ is a characteristic horizontal length scale. It can represent the pool/burner diameter [32, 6, 8], or the entrainment gap of a fixed frame facility [4]. In this work the burner diameter is used was the characteristic horizontal length scale. $\dot{m}$ is the total mass loss (burning) rate of the fuel, $\dot{Q}$ is the total heat release, $\Delta\rho$ and $\Delta T$ are the difference for the ambient density and temperature respectively, $\mu$ is the dynamic viscosity of the gas, $\beta$ is the coefficient of thermal expansion of the gas, $\kappa$ is the thermal conductivity of the gas, and $D_s$ is the molecular diffusion coefficient of species.

The complexity associated with the fire whirl phenomenon is well illustrated with the existence of 13 non dimensional groups [3] that govern the process:

$$\begin{gathered}
\Pi_1 = \frac{U_z}{\sqrt{gH}}, \quad \Pi_2 = \frac{\rho\Gamma}{\mu}, \quad \Pi_3 = \frac{H}{L_h}, \quad \Pi_4 = \frac{\dot{m}}{\rho\sqrt{gL_h^5}}, \quad \Pi_5 = \frac{U_r L_h}{\Gamma} \\
\Pi_6 = \frac{\dot{Q}}{\rho C_p \nabla T U_z L_h^2}, \quad \Pi_7 = \frac{C_p \mu}{\kappa}, \quad \Pi_8 = \frac{\Delta\rho}{\rho}, \quad \Pi_9 = \frac{\Delta T}{T}, \quad \Pi_{10} = \beta T \\
\Pi_{11} = \frac{g\rho^2 L_h^3}{\mu^2}, \quad \Pi_{12} = \frac{U_r}{U_z}, \quad \Pi_{13} = \frac{\rho L_h D_s}{\dot{m}}
\end{gathered} \tag{2.33}$$

Unfortunately, the number of permutations required to investigate the influence of 13 non dimensional groups is prohibitive. Nevertheless, according to [3], in the literature $\Pi_5$ and $\Pi_{12}$ are given far less attention duo to difference in the magnitude order between the radial and tangential components of

velocity. $\Pi_8$ and $\Pi_9$ are also neglected duo to the fact that they are constant for ordinary fires and fire whirls [4].

In this work three non dimensional number are used to analysed the fire whirl phenomenon. The non dimensional heat release is define by

$$Q^* = \Pi_1 \times \Pi_6 = \frac{\dot{Q}}{\rho C_p \nabla T \sqrt{g L_h^3}} \tag{2.34}$$

and the non dimensional circulation by

$$\Gamma^* = \Pi_1 \times \frac{1}{\Pi_5} \times \Pi_{12} = \frac{U_z}{\sqrt{g L_h}} \times \frac{\Gamma}{U_r L_h} \times \frac{U_r}{U_z} = \frac{\Gamma}{L_h \sqrt{g L_h}} \tag{2.35}$$

The non dimensional flame height is defined using $\Pi_3$. Other non dimensional numbers have an important role on fire whirls characterization and understanding such as the swirling number $S$ (eq. 2.36) which quantifies the vortex strength and the Richardson number $R_i$ (eq.2.37), used to quantify turbulence suppression in light of turbulent scales [46].

$$S = \frac{\int_0^\infty \rho v_z v_\theta r^2 dr}{R \int_0^\infty \rho v_z^2 r dr} \tag{2.36}$$

$$Ri = \frac{\frac{2v_\theta}{r} \cdot \frac{\partial (r u_\theta)}{\partial r}}{\left(\frac{\partial u_z}{\partial r}\right)^2 + \left[\frac{r \partial \left(\frac{u_\theta}{r}\right)}{\partial r}\right]^2} \tag{2.37}$$

# Chapter 3

# Implementation

## 3.1 Numerical Model

### 3.1.1 Star-CCM+®

Star-CCM+® was the software used in order to conduct a numerical study of fire whirls as it compiles several packages necessary to perform a numerical simulation such as fluid flow, heat transfer, turbulence, combustion and radiation.

The numerical domain was imported and discretized by the software mesh generator. The volume cells may be generated as tetrahedral, trimmed or polyhedral. Additionally, the software has the option to build prismatic cell layers on wall boundaries. Although in general a polyhedral mesh is less diffusive than a trimmed one, due to the fact that the flow simulated in this case has a dominant direction, an organized mesh such as the one generated by the trimmed model was chosen instead of a polyhedral one. In order to better simulated the effect of velocity gradient and the vorticity production near the wall, the prism layer model was used.

After defined the mesh, the physical models have to be chosen. As mentioned in chapter 2, the problem to be solved is described by the Navier-Stokes equations. This conservation equations can be written in terms of a generic transport equation. The integration over o control volume V leads to the follow generic equation:

$$\underbrace{\frac{\partial}{\partial t}\int_v \rho\phi\partial V}_{\text{Transient term}} + \underbrace{\int_A \rho\phi\cdot\partial a}_{\text{Convection Flux}} = \underbrace{\int_A \Gamma\nabla\phi\partial a}_{\text{Diffusive Flux}} + \underbrace{\int_V S_\phi V}_{\text{Source term}} \tag{3.1}$$

where $\phi$ represents the transport of a scalar property, A is the surface of the control volume and $\partial a$ denotes the surface Vector.

In order to solve the numerical problem, the Finite volume method FVM is used to discretise the equation 3.1 leading to the following equation [47]:

$$\frac{\partial}{\partial t}(\rho\phi V)_0 + \sum_f [\rho\phi(v\cdot a)]_f = \sum_f (\Gamma\nabla\phi\cdot a)_f + (S_\phi V)_0 \tag{3.2}$$

where the convective term $\rho\phi(v \cdot a)$ is equal to the sum of mass flow rate times a scalar on each control volume face being computed with a second order Upwind scheme. The diffusive term is computed with a centre difference scheme.

The Navier-Stokes equations are solved using the iterative solver SIMPLE, introduced by Patankar and Spalding [48, 49]. In the SIMPLE algorithm the solution is found iteratively by generating pressure and velocity fields that consecutively satisfy the momentum and continuity equations [50]. The steps of the algorithm are summarized as follow:

- Update properties $\dot{m}, v, \rho, p$;
- Solve momentum equation;
- Compute the mass fluxes $\dot{m}_f^*$ at faces
- Assemble and Solve pressure correction equation, computing $p'$
- Update the pressure field as $p^{(n+1)} = p^{(n)} + \alpha p'$, where $\alpha$ is the pressure under-relaxation factor
- Compute $m_f^{(n)} = m_f^**, V^{(n)} = V^{**}\rho^{(n)} = \rho^{**}$
- Solve energy, species, turbulence and other scalar equations
- Test for convergence, if it is not converged assume $p = p^*$ and repeat process from step 1

Regarding the physics, the following models were used:

- Ideal gas (multi-component gas)
- Eddy Break Up
- Reynolds Stress Turbulence Transport
- Participating Media Radiation
- Unsteady

The large number of equations associated with the RST model requires special attention on convergence and stability. In order to overcome such difficulties, the simulation was started with the standard $k - \epsilon$ model. Although this model is not suitable for calculating flows with strong swirl and buoyancy it can predict qualitatively the rotating field, being a good initialization for the RST model.

## 3.2 Verification and Validation

In recent years, CFD has became an indispensable tool for most of engineering projects. Wrong decision based on CFD predictions can compromise projects and cancel out the advantages of CFD. The consequences may be the lost of money and wasting of time and effort and in the worst scenario, failure

| Case | Block 1 | Block 2 | Block 3 | Block 4 | Number of cells |
|---|---|---|---|---|---|
| 1 | $3.81 \times 10^{-3}$ | $7.62 \times 10^{-3}$ | $3.05 \times 10^{-2}$ | $1.23 \times 10^{-1}$ | $60439$ |
| 2 | $1.91 \times 10^{-3}$ | $3.81 \times 10^{-3}$ | $1.52 \times 10^{-3}$ | $6.1 \times 10^{-2}$ | $281869$ |
| 3 | $9.53 \times 10^{-4}$ | $1.91 \times 10^{-3}$ | $7.62 \times 10^{-3}$ | $3.05 \times 10^{-2}$ | $1753056$ |
| 4 | $4.76 \times 10^{-4}$ | $9.53 \times 10^{-4}$ | $3.81 \times 10^{-3}$ | $1.52 \times 10^{-3}$ | $11962577$ |

Table 3.1: Details for the 4 mesh cases used. The mesh size are in [m]

of components with drastic consequences. Therefore the necessity to establish rigorous and general methods to evaluate the accuracy and errors from CFD solution has arise. The AIAA guide for verification and validation [51] is an example of an important effort in the creation of rigorous and general methods. The two main principles that are necessary for assessing credibility of CFD simulation are verification and validation.

According to the AIAA guide [51], verification is the process of determining if a computational simulation accurately represents the conceptual model. No attention is given to the fact that the simulation accurately represents the reality or not. The errors are not associated with the wrong choose of physical model, boundaries conditions or even wrong assumptions, instead it is related with discretizations errors, round off or iterative convergence. In this work, a decrease of at least two orders of magnitude on the residuals during a time step was set one of the convergence criteria as well as a constant average value of the variables of interest.

On the other hand validation is the process of determining if a CFD simulation represents accurately the reality. Validation is related with the choose of the right physical models, correct boundary conditions or simplifying hypothesis (for example ideal gas). In order to validated a CFD code, experimental measurements are necessary.

### 3.2.1 Verification

In order to obtain a satisfactory numerical error, a convergence analysis is performed. The computational domain was discretized with trimmed cells. The relative simple geometry and the existence of a dominant direction on the flow dictated the choice of a simpler mesh generation such as a trimmer one instead of a more complex one such as polyhedral one. The mesh comprises four different blocks with refinement (see figure 3.1 a)) with the purpose of correctly predict the large gradients on the flame, optimizing the total time required to run a simulation, see figure 3.1. Prism layers were used on the bottom boundary as well as on the inner cylinder walls for better discretization of high gradients on the formation of fire whirls and vorticity production. The analysis is performed for a $5$ kW dimethil ether fire whirl. Details of the simulation setup are presented and discussed on the next subsection.

Table 3.1 lists the details of the 4 mesh cases used to perform the convergence analysis. For the sake of simplification, the mesh refinements were obtained decreasing to half of the size used on the previous mesh. One should note that all mesh cases used 10 layers and prism layer thickness used was $6.25\%$ of the mesh size of block 4. Figure 3.2 a) shows the flame height obtained and respectively error as function of the number of cells used. The error was calculated using the experimental observations of Hartl and Smits [4]. There is a considerable improvement on the obtained flame height for around 1.8

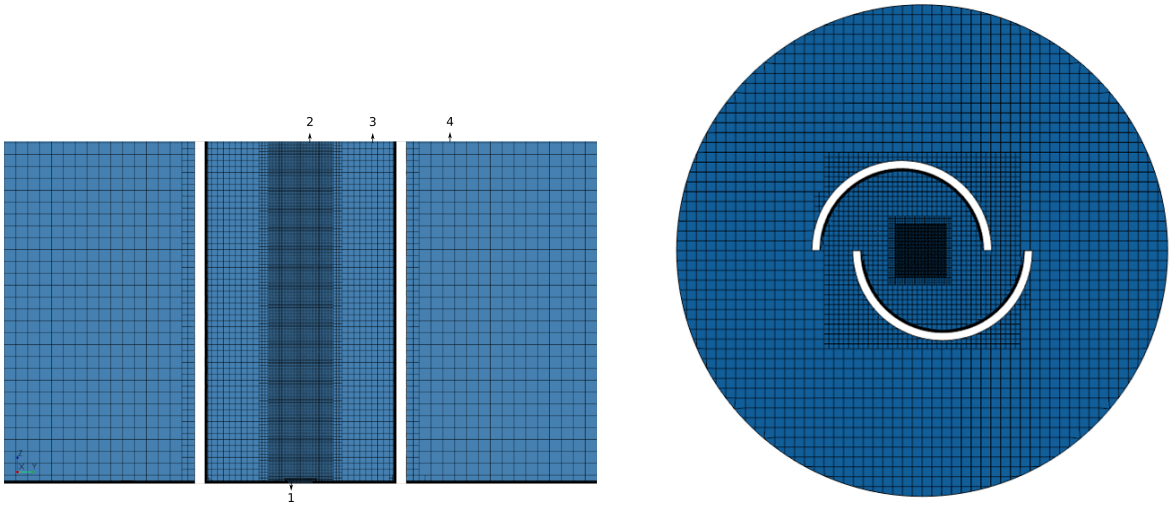


(a) Front view (b) Top View

Figure 3.1: Example of the generated mesh. Figure a) shows the location of the different block with refinement

million cells. However little improvements is observed between 1.8 million and 12 million cells. Figure 3.2 b) shows the obtained circulation, using the Stokes theorem as function of the number of cells used. The observations are fairly similar to flame height. Figure 3.3 shows the vorticity radial profile for the 4

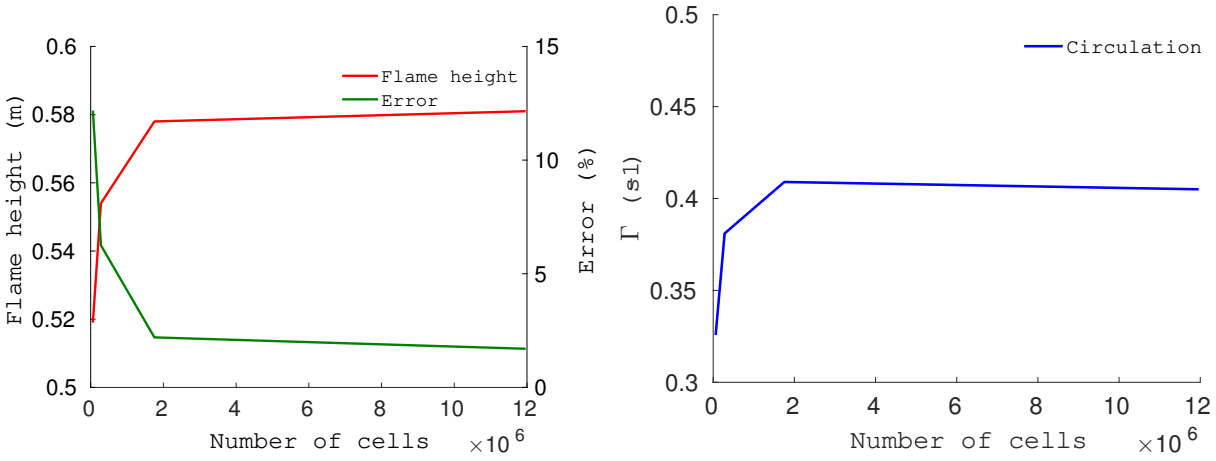


(a) Flame height and corresponding error (b) Circulation

Figure 3.2: Obtained flame height and circulation as function of number of cells

meshes. As for the flame height and circulation results, there is a considerable improvement observed on the simulation results between mesh 1 and 3. The improvement observed for mesh 4 compared with mesh 3 is almost neglectable, consistent with the results obtained for circulation. Additionally, it was observed that for mesh 1 and 2 the fire whirl was not centred with the burner, in contrast to the fire whirl obtained with mesh 3 and 4. This is consequence of the lack of resolution on the fire whirl generator slits obtained with mesh 1 and 2. Although the improvements between mesh 1 and 2 are considerable, they proved insufficient.

Figure 3.4 a) shows the temperature radial profile obtained with the 4 meshes analysed. Once again it is visible that the obtained fire whirl for mesh 1 and 2 is not centred. Additionally, mesh 1 results in

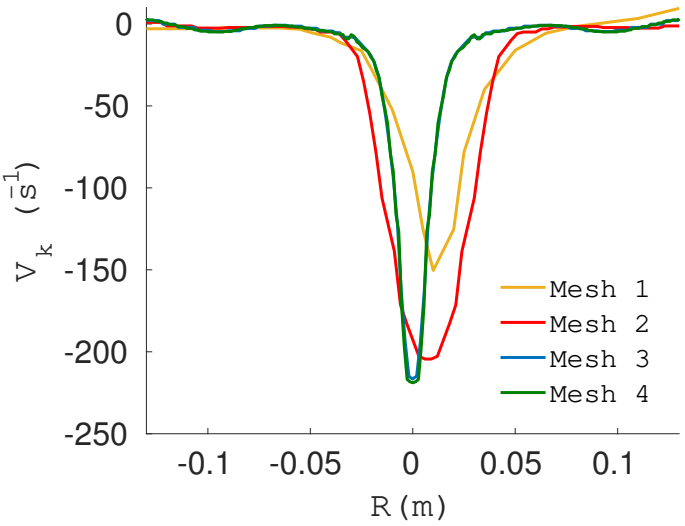


Figure 3.3: Vorticity radial profile for all meshes cases

a maximum temperature located on the core the fire whirl, indicating lack of resolution on the fire whirl core, contrary to mesh 2, 3 and 4, that predicted the maximum temperature on the flame front. The profiles obtained for mesh 3 and 4 are fairly similar. Figure 3.4 b) shows the computed radial profile for the axial velocity. The profiles obtained for mesh 1 and 2 suggest that both mesh result on poor resolution on the fire whirl core. For mesh 3 and 4 the profiles are similar.

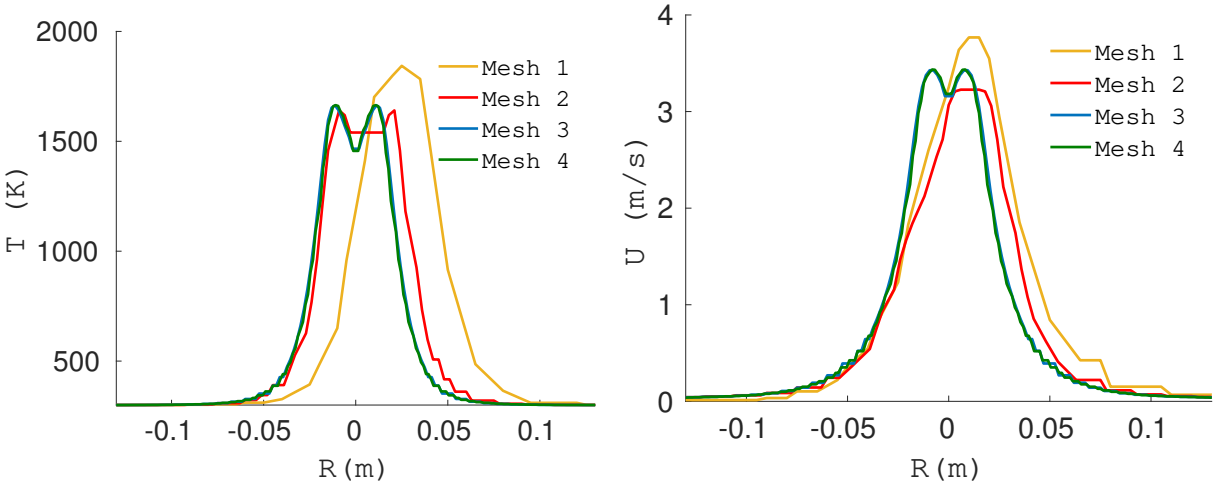


(a) Temperature radial profile

(b) Radial profile of axial velocity

Figure 3.4: Obtained radial profiles for temperature and axial velocity

The previous analysis show that $60439$ and $281869$ cells are not enough to obtain the required numerical error and mesh independence. The profiles obtained for 1.8 and 12 million, as well as the flame height and circulation results show that the improvement obtained for 12 million cells does not compensate the computational cost associated, dictating the choice of mesh 3 to study fire whirls.
Finally, note that for mesh 3, the mesh size for block 2 is 20 times smaller than the burner diameter. The mesh used for different fire whirl generators dimensions is based on this principle.

### 3.2.2 Validation

Figure 3.6 shows the fire whirl generator geometry comprising two half staggered cylinders located at the centre of the computational domain. The facility dimensions are listed on table 3.3. The origin of the Cartesian coordinate system is centred at the base of the burner.

Figure 3.5 shows the burner geometry used in simulations. The burner modelling is similar to the one used by Lei *et al.* [52]. A mass flow inlet with the fuel mass fraction set to one is used and the porous media was modelled with (pressure drop) source terms on the momentum equation. Two types of gaseous fuels were used, dimethil ether was used for $2kW$ and $5kW$ simulations and propane was used for the $50kW$, $150kW$ and $300kW$ simulations. Table 3.2 lists the properties of the used fuels. The far

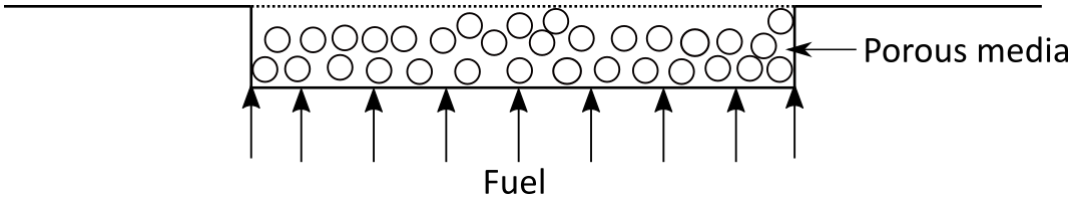


Figure 3.5: Detail view of the burner

| Fuel | Chemical Formula | $\rho$ [$Kg/m^3$] | LHV [$MJ/Kg$] |
|---|---|---|---|
| Dimethil ether | $C_2H_6O$ | 2.11 | 28.882 |
| Propane | $C_3H_8$ | 2.01 | 46.296 |

Table 3.2: Properties of the fuels used

| Heat release [kW] | $D_0$ [m] | $D$ [m] | $S$ [m] | $H$ [m] |
|---|---|---|---|---|
| 2 | 0.0381 | 0.305 | 0.0762 | 0.890 |
| 5 | 0.0381 | 0.305 | 0.0381 | 0.890 |
| 50 | 0.3 | 2 | 0.4 | 15 |
| 150 | 0.3 | 2 | 0.4 | 15 |
| 300 | 0.3 | 2 | 0.4 | 15 |

Table 3.3: Geometry details for simulated cases

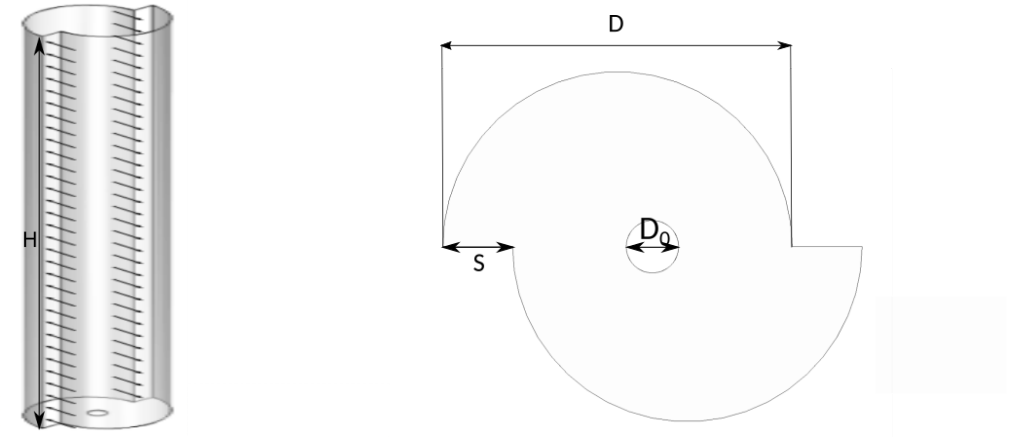


(a) Geometry used (b) Top View

Figure 3.6: Fire whirl generator

field boundary were modelled as pressure outlet with prescribed pressure ($p_{working} = p_{static} - \rho_{ref} \cdot g \cdot dh$) set to zero relative to the atmospheric pressure. The no slip boundary condition was assigned to all physical walls.

### Turbulence Models

The prohibitive computational cost of solving directly the governing equations (DNS) and the considerable cost of using filtered quantities (LES) dictates the selection of RANS. It is well know the lack of performance of two equation turbulence models as $\kappa - \epsilon$ to simulate flows dominated by buoyancy and swirl, see e.g, Hanjalic [35] and Pereira and Rocha [36, 37].
Nevertheless, three turbulence models available on Star-CCM+®, RST, standard $\kappa - \epsilon$ and LAG Elliptic $\kappa - \epsilon$ were tested in order to evaluate their performance regarding fire whirls simulations.
Figure 3.7 shows the flame stoichiometric mixture fraction used to calculate the flame height. The difference between the RST and both $\kappa - \epsilon$ is very large, being the predicted RST close to the one reported by [52] which is $4.33$ m, and it is around 2.6 times greater than both $\kappa - \epsilon$ models prediction. The modifications presented on the LAG EB $\kappa - \epsilon$ had little effect concerning flame height.


Figure 3.7: Predicted flame height for the three turbulence models

The lack of performance of two equations is also clear analysing the predicted velocity fields. Both the standard and LAG EB $\kappa - \epsilon$ fail to predict correctly the tangential velocity field as show in figures 3.8 and 3.9. Both standard and modified $\kappa - \epsilon$ (figure 3.8.A) 3.8.B)) predicted a much larger vortex radius. In contrast, figure 3.9 shows that the RST model predicted a tangential velocity field in close agreement with the experimental data from several authors [4, 52].

Figure 3.10 shows the turbulent kinetic energy field for a) standard $\kappa - \epsilon$, b) LAG EB $\kappa - \epsilon$ and c) RST model. Both $\kappa - \epsilon$ models predicted larger values of turbulent kinetic energy on the flame zone than the RST model. The larger values of turbulent kinetic energy for the $\kappa - \epsilon$ models confirms the lack of performance of two equations turbulence model. Such models usually overpredict turbulence for flows dominated by swirling and buoyancy [19]. The much larger values predicted by both $\kappa - \epsilon$ are related with a smaller flame height prediction. The high values are associated with an increase of turbulent mixing

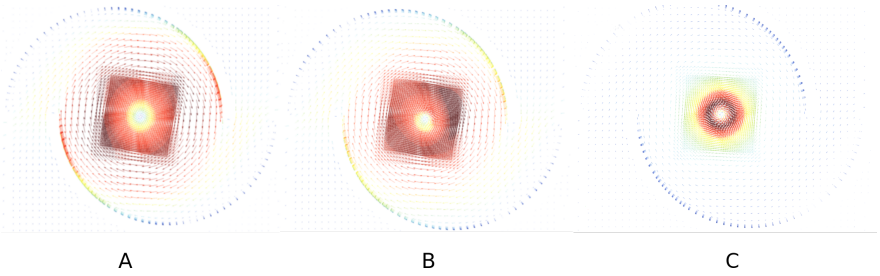


Figure 3.8: Predicted tangential velocity fields for $z = 1.2m$.

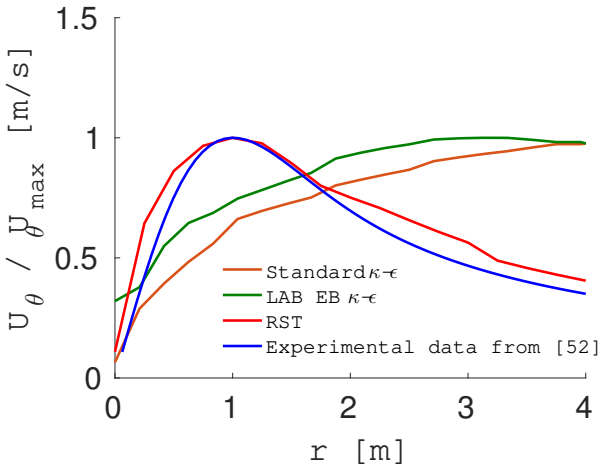


Figure 3.9: Predicted tangential velocity profiles of the three turbulence models and experimental data from [52]

of fuel with the entrained air. Consequently the increase on turbulent mixing requires a smaller flame surface and consequently a smaller flame height. Furthermore the Eddy Break-Up takes into account the effect of turbulence on the reaction rates which are function of the turbulent kinetic energy. Higher $\kappa$ values represent greater reaction rates and consequently smaller flames heights.

**Validation with available experimental data**

The numerical simulations were validated with experimental data obtained in fire whirls by Hartl and Smits [4] and Lei *et al.* [52]. They were obtained for different inlet burners heat releases ranging from $2$ to $300$ kW, and two different fuels, dimethyl ether ($2$ and $5$ kW) and propane ($50$, $150$ and $300$ kW). This range of heat releases allows the validation on an important range (three orders of magnitude) of power. Figure 3.11a) shows the predicted mixture fraction stoichiometric isosurface for $300$ kW around the cylindrical fire whirl with 15 burner diameter in height together with the spiral streamlines configuration. The predicted flame shape is in agreement with the observations by visual inspections of [4, 20, 52]. Figure 3.11b) shows a radial profile of the tangential velocity compared with an analogous profile from the analytical solution of a Burgers vortex. The obtained good agreement suggest that the Burgers vortex describes well the flow kinematics in agreement with other authors [4, 52, 31, 38].

Figure 3.12 shows the comparison between the predicted and measured maximum tangential velocity along the fire whirl height. The maximum tangential velocity, $V_m$, tends to be constant or increase

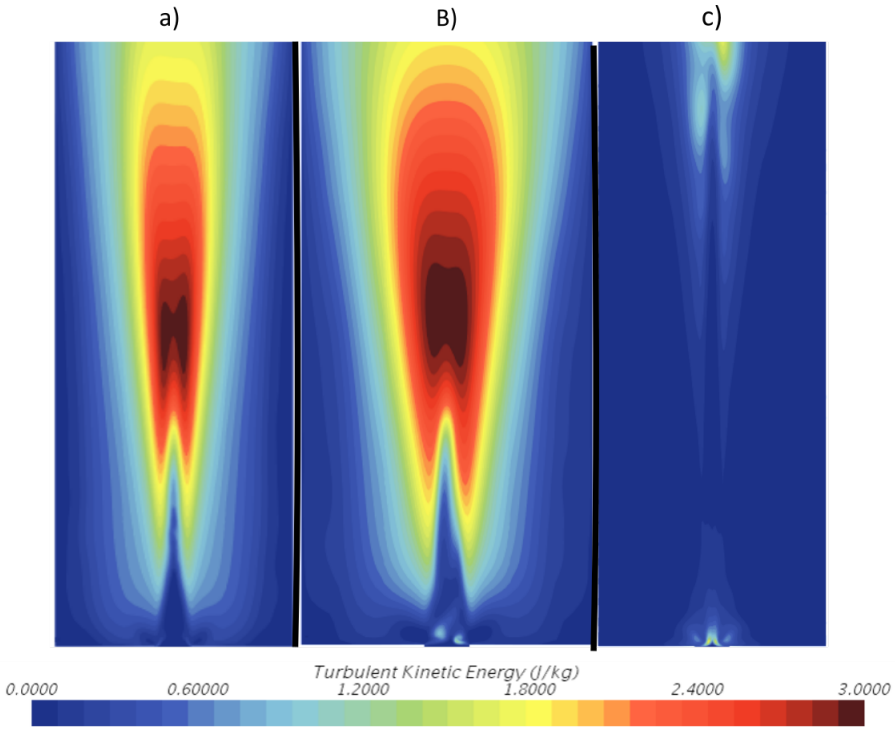


Figure 3.10: Predicted kinetic turbulent energy for a) standard $\kappa - \epsilon$, b) LAG EB $\kappa - \epsilon$ and c) RST model.

slowly until $\frac{z}{D} = 1.25$, and then decreases with height, as observed in the experimental work of Lei *et al.* [52]. Figure 3.13 shows the predicted and measured, Lei *el al.* [52], centreline excess temperature profile $(T - T_0)$. The numerical simulations are in agreement with the experiments up to the over fire plume zone. The same behaviour is present on the normalized centre line axial velocity (figure 3.14).The location where the velocity and temperature decrease correspond to the plume origin and the difference between prediction and measurements is attributed to temporal oscillations of the plume origin.

Small, $q = 2$ kW, fire whirls where also predicted and figure 3.15 shows the three velocity components along a radial profile at $z/H = 0.2$. The obtained results agree well with the experimental observations from [4].

Table 3.4 lists the corresponding measured and predicted flame height for $2$, $5$, $50$, $150$ and $300$ kW. The experimental continuous flame height is based on the location of the maximum centreline axial velocity. The criterion used in the numerical simulations is based on the stoichiometric mixture fraction that is consistent with experimental criterion. One should note that the measured flame height estimated from visual inspection of the flame is different from the value obtained by the location of time average centerline maximum axial velocity [52]. If the reference experiments are based on the average visual inspection, the error between the prediction and experiments are typically 15% in the range from $50$ to $300$ kW. Regarding circulation, the obtained values were compared with the experimental data from [4]. Circulation was calculated using the Stokes obtained at cross planes integration of vorticity. Figure 3.16 shows the variation of circulation along a small power ($5$ kW) fire whirl. The circulation above the fire whirl entrainment region is nearly constant along the fire whirl height, consistent with the observations of [4]. Table 3.5 lists the corresponding measured and predicted circulation for 2 and $5$ kW. The predictions

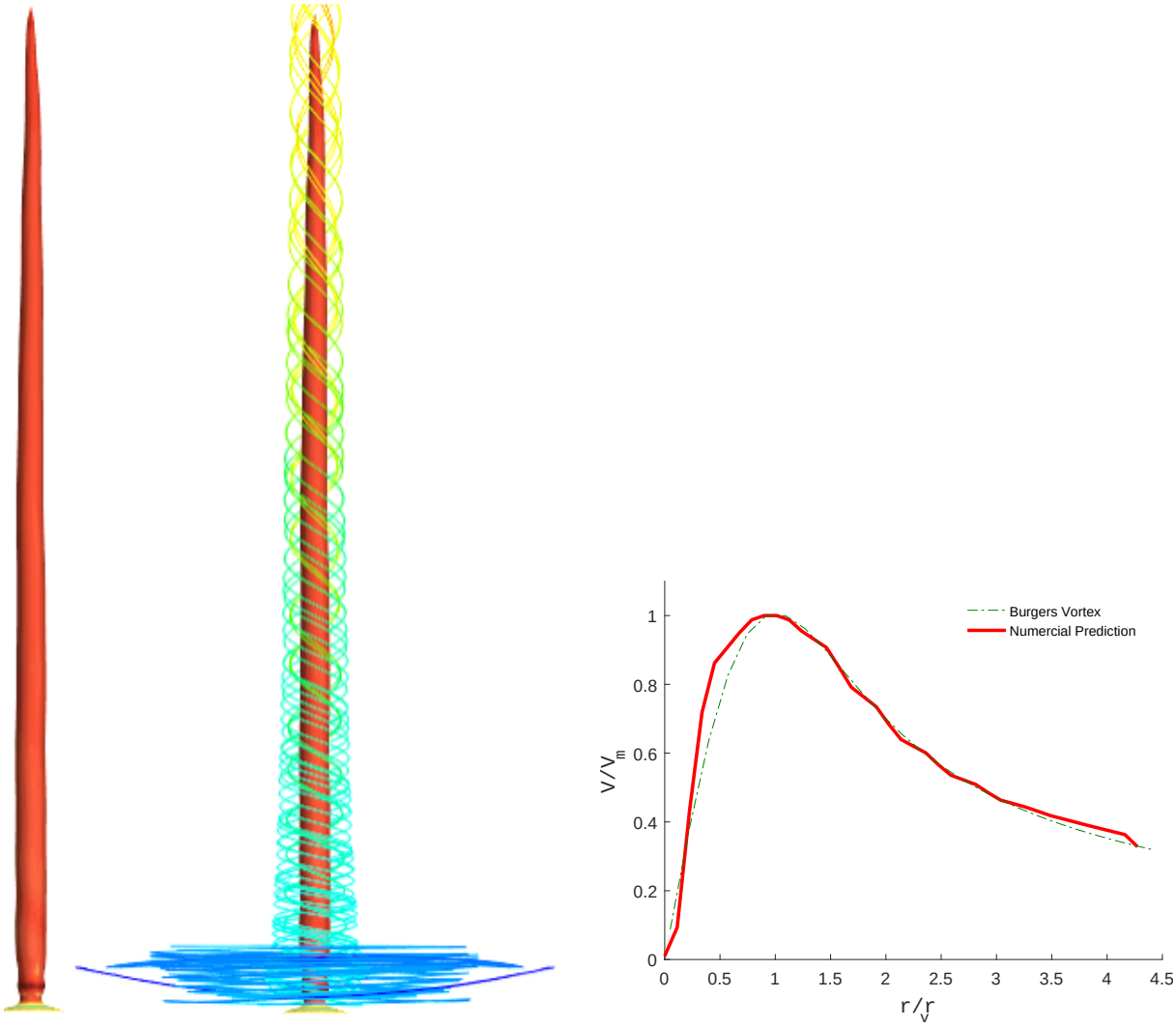


(a) Stoichiometric mixture fraction isosurface

(b) Radial velocity profile for 300 kW

Figure 3.11: Isosurface of stoichiometric mixture fraction and predicted tangential velocity profile

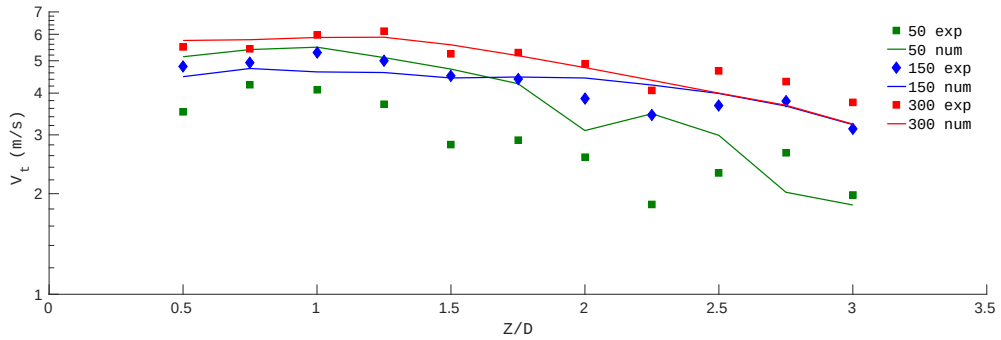


Figure 3.12: Numerical and experimental maximum tangential velocity versus height

| Heat release [kW] | Experimental [m] | Numerical [m] | Error % |
|---|---|---|---|
| 2 | 0.347 | 0.362 | 4.32 |
| 5 | 0.591 | 0.578 | 2.20 |
| 50 | 1.31 | 1.33 | 1.53 |
| 150 | 3.19 | 3.31 | 3.76 |
| 300 | 4.33 | 4.45 | 2.77 |

Table 3.4: Flame height prediction and comparison with experimental data

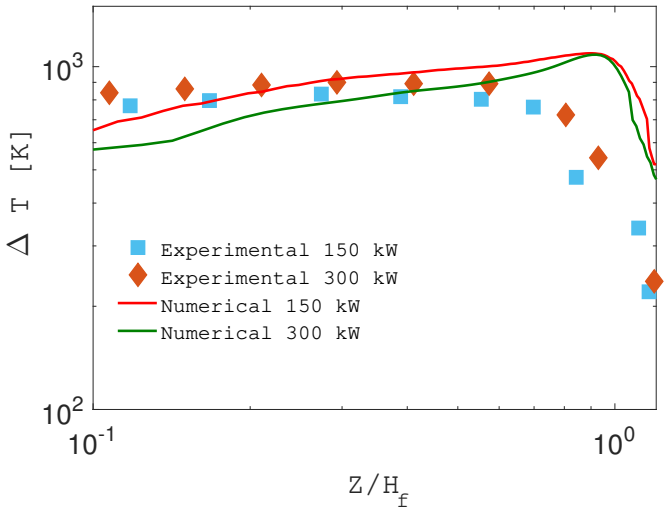


Figure 3.13: Centreline temperature profile

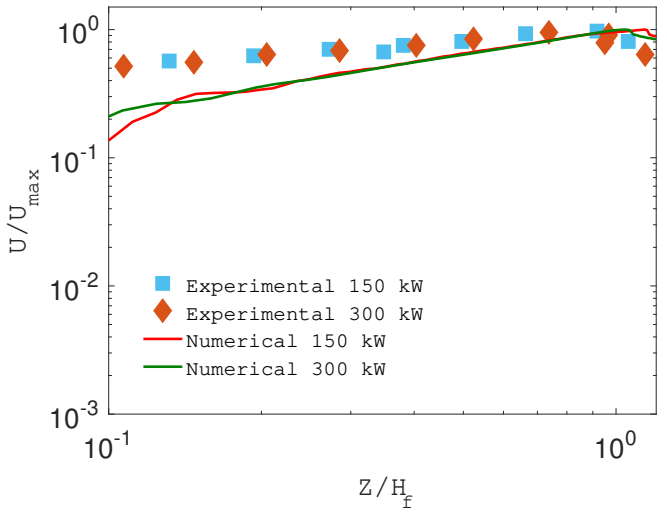


Figure 3.14: Centreline axial velocity profile

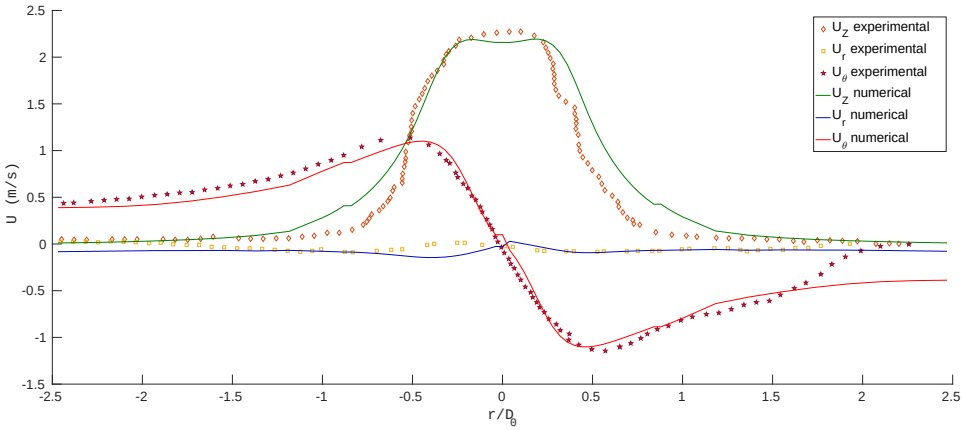


Figure 3.15: Axial, tangential and radial velocity profiles for $q = 2kW$.

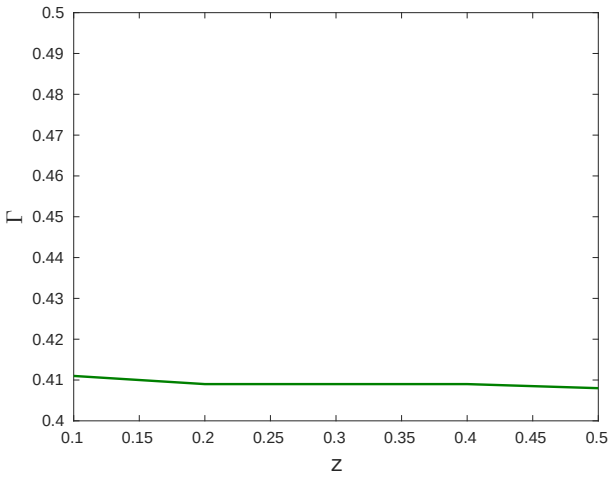


Figure 3.16: Circulation vs height for $5$ kW

are is satisfactory agreement (maximum error of $10\%$) with the available experimental observations.

| Heat release [$kW$] | Experimental[$m^2/s$] | Numerical[$m^2/s$] | Error % |
|---|---|---|---|
| $2$ | $0.262$ | $0.235$ | $10.3$ |
| $5$ | $0.387$ | $0.409$ | $5.68$ |

Table 3.5: Circulation comparison with data from [4]

# Chapter 4

# Results

In this chapter the effect of circulation on the flame structure is discussed. For each non-dimensional heat release the open-boundary condition of constant hydrostatic pressure far away from the facility allows to predict implicitly the mass flow entrainment through the facility slits. These numerical set-up correspond to the natural process occurring in the laboratory and will be denominated as ”naturally aspired”. To cover a wider range of circulation other conditions denoted as ”prescribed mass flow” are simulated. These ”prescribed mass flow” correspond to prescribe the mass flow rate directly in the slits facility.
This chapter is organized as follows: Firstly the difference and consequences of ”naturally aspirated” and ”prescribed mass flow” is discussed. Secondly the circulation as function of the gap width is analysed for the ”naturally aspirated” case. Finally, the effect of circulation on the flame structure is discussed. A correlation os flame height as function of circulation is presented and discussed.

## 4.1 Naturally aspirated and prescribed mass flow rate

For the heat releases of $150$ and $300$ kW, the implicit mass flow entrainment was calculated. Table 4.1 lists the mass flow obtained for each case. The predicted velocity along the centreline of the experimental facility gap in not constant with height, consistent with the observations of [52]. Figure 4.1 shows the difference on the velocity along the centreline of the gap for the ”naturally aspirated” case and ”prescribed mass flow” one. Initially for the ”naturally aspirated”, it decrease with height until z=4 where as increase in the velocity observed. For z=7 the velocity decrease with height. In contrast, the ”prescribed mass flow” is obtained setting a constant velocity along the experimental facility gap height.

| Heat release (kW) | Gap $S$ [m] | $\dot{M}$ [kg/s] |
|---|---|---|
| 150 | 0.4 | 2.84 |
| 300 | 0.4 | 3.61 |

Table 4.1: Mass flows for naturally aspirated $150$ and $300$ kW cases.

Figure 4.2 shows the numerical predictions of flame height and circulation obtained with ”naturally as-

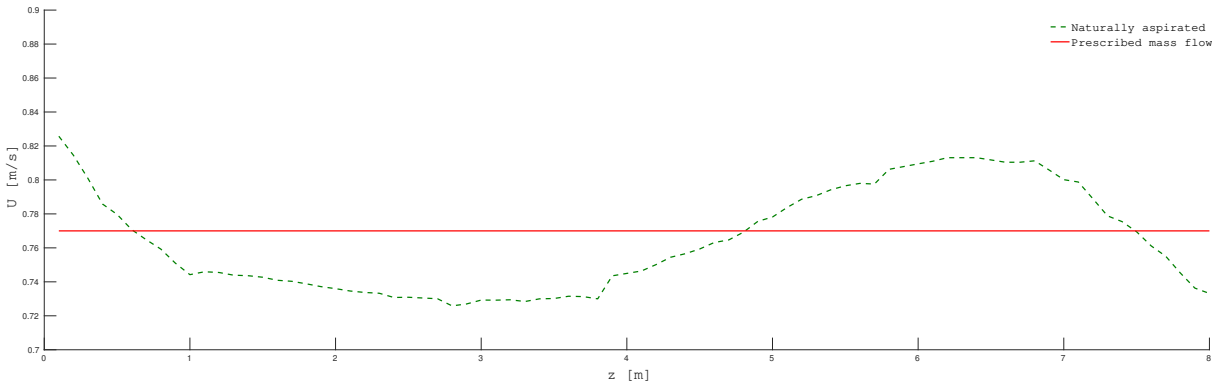


Figure 4.1: Difference between ”prescribed mass flow” and ”naturally aspirated” one for $150$ kW.

pirated” and the analogous ”prescribed mass flow” one. For both fuel rate supplies considered, the ”prescribed mass flows” results on an under prediction of circulation 4.2b) and consequently the flame height is smaller, see figure 4.2 a). Such predictions suggest that circulation not only depends on the mass flow entering on the fire whirl generator, but also on the velocity profile on the facility gaps.

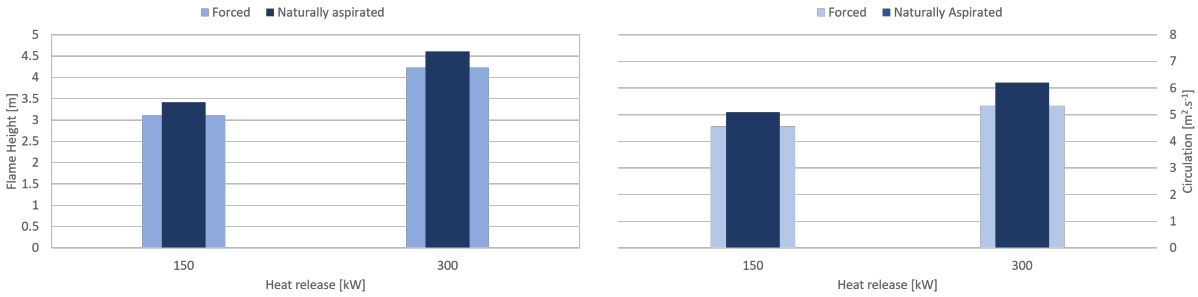


(a) Flame height

(b) Circulation

Figure 4.2: Numerical prediction of flame height and circulation for ”prescribed mass flow” and ”naturally aspirated” cases

The difference between the ”naturally aspirated” and ”prescribed mass flow” is mainly due to the differ-

(a) Naturally aspirated

(b) Prescribed mass flow

Figure 4.3: Predicted isosurfaces for mixture fraction and Q-criterion

ence on thye velocity near the ground layer of the facility. This greater velocity gradient results on larger vorticity production on the floor consequently increasing the vortex circulation. Figure 4.4 shows the wall

shear stress for both cases. The natural aspirated case, presents a greater shear stress, mainly near the burner edge. Additionally figure 4.3 shows that there is little difference on the flame structure The main difference is that the predicted flame and plume with the mass flow boundary condition exhibits less oscillations and is more stable, consequence of the uniformisation of the tangential entrainment.

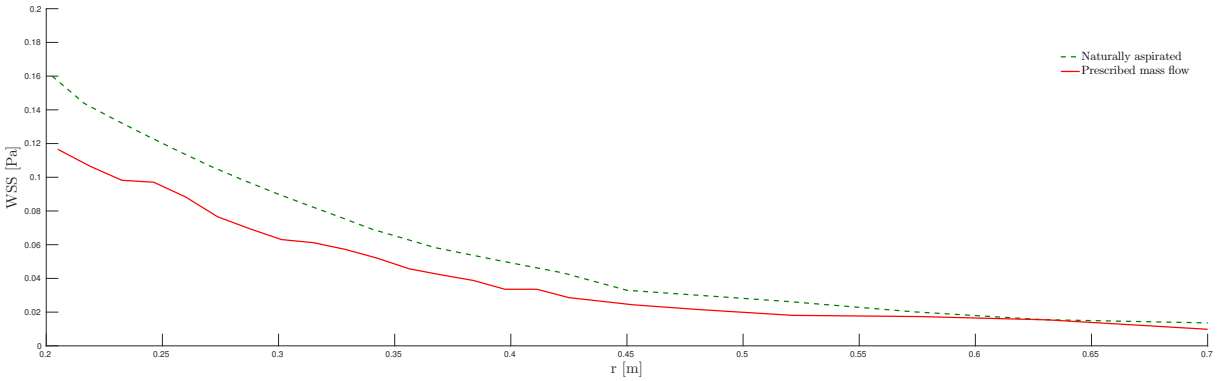


Figure 4.4: Predicted wall shear stress for forced mass flow and natural aspirated case

## 4.2 Gap variation

The variation of circulation on the ”naturally aspirated” case was obtained increasing or decreasing the facility gap width, similar to the approach of [4]. 3 gaps widths were used, $30$ cm, $40$ cm and $60$ cm. The reduced number of different gap widths is consequence of geometry constrains. For instance, the decrease of gap implies an increase in circularity, in contrast to the increase of the gap width that decreases the circularity of the facility, leading to an elliptic shape for wider gaps. With that in mind, the 3 gaps mention before, were chosen in order to maximize the range of gap variations without a considerable impact on the overall facility geometry. Note that in order to keep fairly constant the minimum mesh resolution for all gaps, a mesh refinement on the facility gap zone was applied for the case of $S = 0.3$ m.

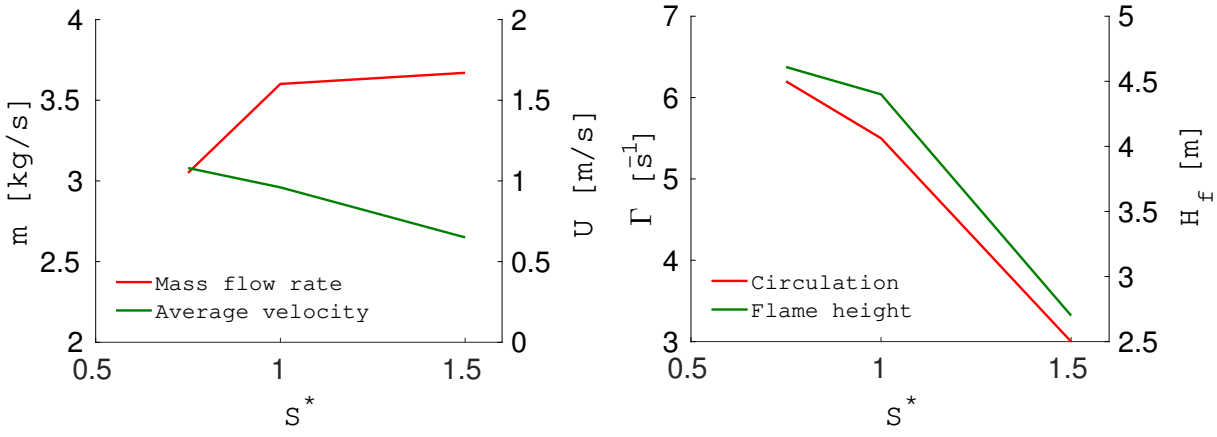


(a) Mass flow and average velocity

(b) Circulation and flame height

Figure 4.5: Numerical predictions for gap mass flow, velocity, circulation and flame height function of normalized gap

Figure 4.5a). shows the entrainment mass flow and velocity as function of the gap width and figure 4.5b). shows the circulation and flame height as function of the gap width. The horizontal axis represent the gap width normalized by the gap width used in the validation case studies, $S = 0.4$ m.

$$S^* = \frac{S}{S_4} \tag{4.1}$$

On one hand the mass flow increases with the increase of the gap width. However this increase on mass flow does not generate an increase on the entrainment momentum as illustrated on figure 4.5 a). Contrary to the mass flow, the average velocity increases with the decrease of gap width, leading to an increase in circulation and consequently flame height. The previous analyses indicates that the momentum and velocity profile have a greater impact than the mass flow across the gap facility on circulation, which is consistent with the conclusion derived on section 4.1.

## 4.3 Circulation effect on flame

### 4.3.1 Flow Pattern

A typical fire whirl calculation for P=$300$ kW is presented in figure 4.6 a) that shows isocontours of the mean temperature and velocity vector in the flame vertical cross section. The maximum flame temperature is located at the shear layer near the flame origin while the centre of the fire whirl has a relatively lower temperature T=$600$ K, indicating a rich fuel zone. The gas burner inlet porous configuration located

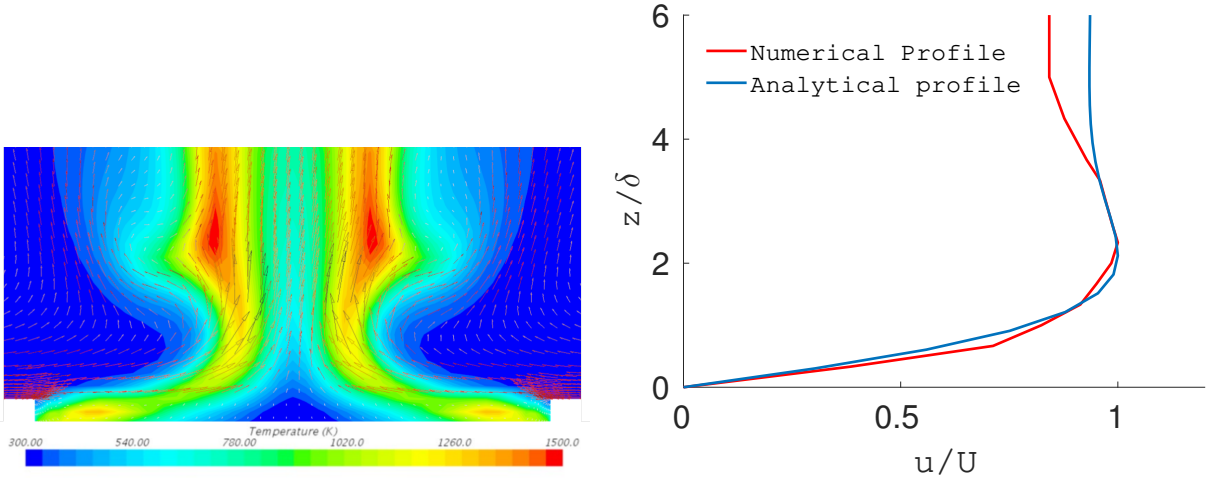


(a) Isocontours of temperature and velocity vectors

(b) Velocity profile

Figure 4.6: Predicted flame shape and flow patterns

below the fire whirl ground level allows for a natural influence of the air swirl on the low momentum inlet fuel jet with Reynolds number ($Re = \frac{UD_0}{\nu}$) equal to 2702. As a consequence, figure 4.6 a) shows a fuel jet behaviour similar to a pool fire with the narrowing conical shape of the fuel. This shape is consistent with an existence of an Ekman type inflow boundary layer [1, 3]. Figure 4.6 b) shows that the predicted velocity profile on the boundary layer over the ground floor is in agreement with an Ekman layer solution.

The Ekman solution is an exact solution of the Navier-Stokes equations only valid for laminar flows. For turbulent flows there are two parameters in the analytical solution to be carefully evaluated, $k_m$ and $\delta$, being $k_m$ the kinematic viscosity and $\delta = \sqrt{\frac{2K_m}{f}}$ the Ekman layer thickness, assuming a constant turbulent "eddy" viscosity, $k_m$ and assuming the Coriolis parameter $f = \frac{2\pi}{T}$ with the period $T$ obtained by the tangential velocity. The turbulent eddy viscosity was assumed to be given by $\nu_t = C_\mu \frac{\frac{1}{2} * (\overline{u'^2} + \overline{v'^2} + \overline{w'^2})}{\epsilon}$ with $\epsilon$ the turbulent dissipation rate and $C_\mu = 0.09$. The eddy viscosity is almost constant across the location of the Ekman layer and the prediction allow to estimate the modelled parameters as $k_m = 0.005 m^2/s$, $f = 1.8 s^{-1}$ and $\delta = 0.07 m$. In spite of the gross assumption of the eddy diffusivity, $\delta$ was surprisingly in satisfactory agreement with the analytical Ekman solution as shown in figure 4.6 b).

Figure 4.7 shows the vorticity in the perpendicular plane for three different circulation, $\Gamma^*$, values and $Q^* = 0.68$. The vorticity field supported the flow pattern visible on figure 4.6 a) where the promoted inflow layers shrink the flame. This shrink creates a considerable curvature on the base flame. This pattern visible on figure 4.6 a) with velocity vectors is support by highest vorticity values on the fire whirl on the fire whirl base, indicating the presence of large velocity gradients. The vorticity present above the previously mentioned vorticity zone are consequence of the flame expansion that forces the flow to contour the flame. The curvature created by the flame expansion is expressed on the vorticity generation.

The two approaches used to generate circulation, "prescribed mass flow" and "naturally aspirated", were considered for each non dimensional heat release $Q^*$ obtained from dimensional analysis and derived from the $\Pi$ non dimensional groups [3].

$$Q^* = \Pi_1 \times \Pi_6 = \frac{\dot{Q}}{\rho C_p \nabla T \sqrt{g L_h^3}} \tag{4.2}$$

Analogously, for $\Gamma^*$ the same procedure yields:

$$\Gamma^* = \Pi_1 \times \frac{1}{\Pi_5} \times \Pi_{12} = \frac{U_z}{\sqrt{g L_h}} \times \frac{\Gamma}{U_r L_h} \times \frac{U_r}{U_z} = \frac{\Gamma}{L_h \sqrt{g L_h}} \tag{4.3}$$

Vorticity generation increases with the increase of the circulation, $\Gamma^*$, suggesting that circulation promotes greater curvature and radial inflow. The increase of velocity on the fire whirl base increase the velocity gradients and consequently increase the generation of vorticity. Figure 4.8 shows isocontours

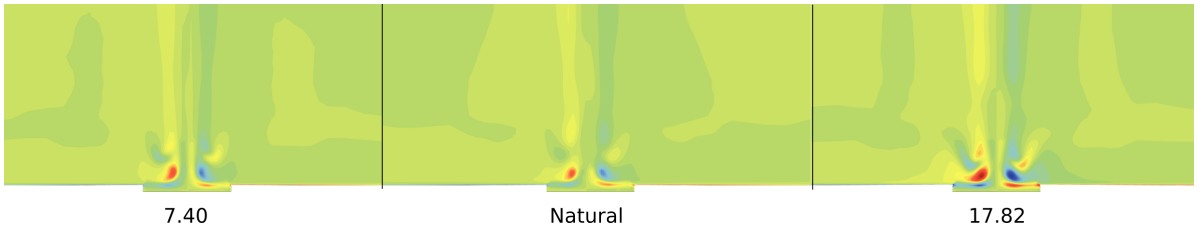


Figure 4.7: Isocontour of vorticity

of the mean temperature and velocity vector for the analogous non swirling flame a) and a fire whirl b). The non swirling flame presents a typical conical shape, starting on the burners edges, contrary to fire

whirl flow pattern which is similar to a pool fire. Contrary to the fire whirl, the analogous non swirling flame does not have a expansion zone on the flame base. The lack of expansion zone is well evident by the lack of curvature and shear layer on the flame base. Consequently, the maximum temperature on the analogous non swirling flame does not occur on the flame base contrary to the fire whirl.
Finally, the previous inflow layer present on the fire whirl does no exist on the non swirling analogous flame, justifying the flame shape.

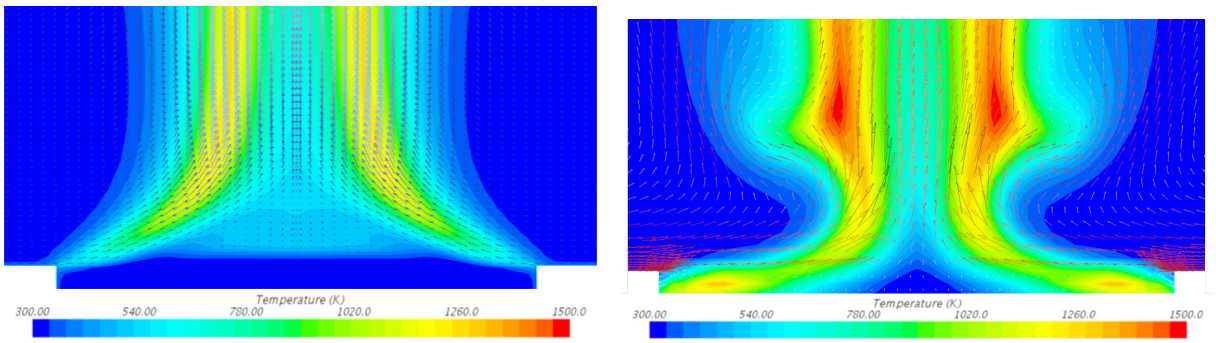


(a) No swirling flame

(b) Fire whirl

Figure 4.8: Predicted flame shape and flow patterns for $300$ kW non swirling flame and analogous fire whirl

### 4.3.2 Flame Height

The open literature and the previous results support the strong dependence of circulation on flame height. According to the Stokes theorem, the circulation is the integral of the vorticity field, consequently, increasing the tangential momentum at the facility slits increases the vorticity field. To study the sensitivity of the fire whirl height to tangential air entrainment three burner heat releases ($5$, $150$ and $300$ kW) were considered. According the powers considered in this work of ($5$, $150$ and $300kW$) are equivalent to $Q^* = 4.63$,$0.69$ and $1.37$ respectively. One should note that the lowest power correspond to the highest non dimensional heat release. For each non-dimensional heat release the open-boundary condition of constant hydrostatic pressure far away from the facility allows to predict implicitly the mass flow entrainment through the facility slits. These numerical set-up correspond to the natural process occurring in the laboratory and will be denominated as "naturally aspired". To cover a wider range of circulation other conditions denoted as "forced entrainment" are simulated. These "force entrainment" correspond to prescribe the mass flow rate directly in the slits facility.
Figure 4.9 shows the non-dimensional flame height $H^* = \frac{H_f}{D_0}$, ($D_0$ being the burner diameter) as a function of the non-dimensional circulation. For each non dimensional heat release it was predicted that the maximum flame height is reached for the "naturally aspirated" solution. The existence of a critical circulation is in agreement with the observation of [18], [19] and [20].
The present results comprises gaps with different sizes and the flame height trend is common to slightly decrease with forced mass flow in excess to the natural aspired value at the facility slits. The decrease in flame height is attributed to a more rapidly fuel consumption at the fire whirl base as will be described forward.

The predicted fire whirl height was correlated with the circulation considering only the "naturally as-

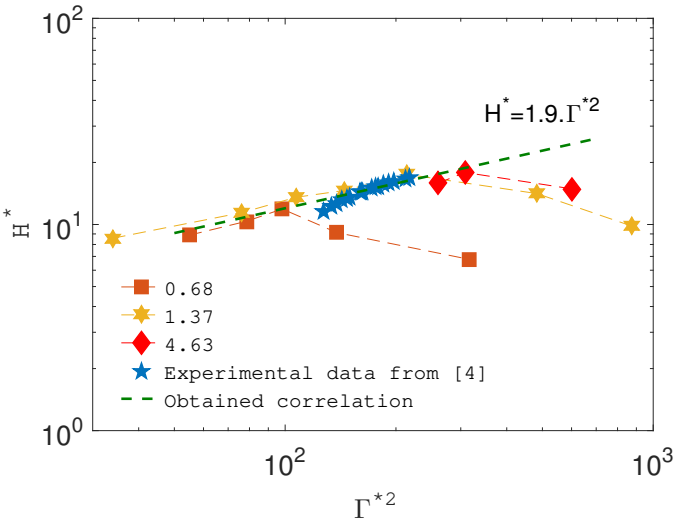


Figure 4.9: Correlation curve of fire whirl height $H^*$ versus circulation $\Gamma^*$obtained from predictions and experimental data from [4]

pirated" data and the data from [4]. The obtained correlation expressed by $H^* = 1.9\,(\Gamma^*)^{0.8}$ shares a similar slope with the one derived by Kuwana *et al.* [5], obtained from the numerical predictions of [18]. Figure 4.10 shows the isocontours of radial velocity on the fire whirl base. It is observed that the highest $\Gamma^*$ value induces a greater radial velocity, suggesting an intensification of the promotion of the radial inflow with circulation. This is very important to the flow patterns that have to go around the flame expansion creating a wavy rotating stream around the fire whirl root.

Figure 4.11 shows the non-dimensional fuel mass flow $\dot{M}^* = \frac{\dot{m}}{\dot{m}_0}$ as a function of height, obtained by integration of fuel concentration at several cross planes. The fuel consumption increases with circulation on the fire whirl base, suggesting an increase of air entrainment due the radial velocity component enhancement. The increase air entrainment and consequently fuel consumption has as consequence the flame shortening observed for forced mass flows in excess to the natural aspired value at the slits port.

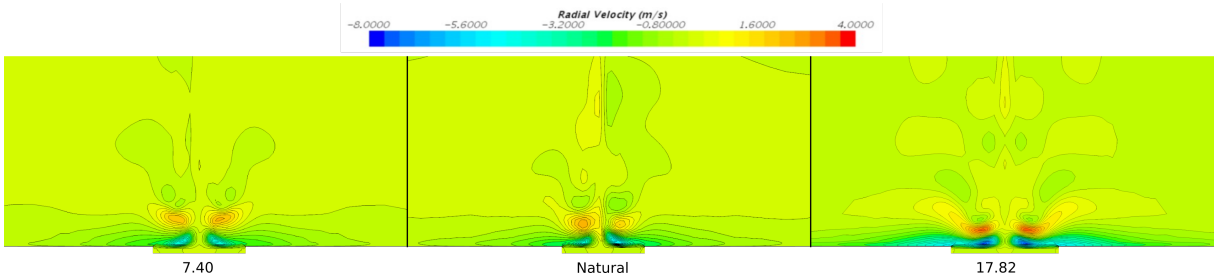


Figure 4.10: Isocountours of radial velocity on the fire whirl base for three circulation values

The "naturally aspired" cases for $150$ and $300$ kW flame height were compared with analogous non swirling flames. Table 4.2 list the continuous flame height predicted for both fire whirl and analogous non swirling flame. The predicted continuous flame height for fire whirls is around twice of the one obtained

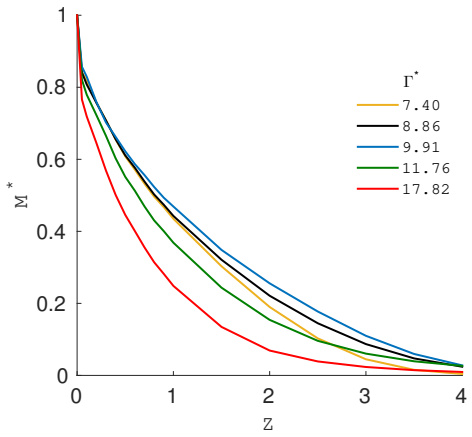


Figure 4.11: Non dimensional fuel mass flow vs height for 5 circulation $\Gamma^*$ values

for analogous non swirling flame. This result support the statements from [53, 52].

| | Flame height [m] | |
|---|---|---|
| Heat release [kW] | Non swirling | Fire whirl |
| 150 | 1.63 | 3.31 |
| 300 | 2.25 | 4.45 |

Table 4.2: Flame height [m] predicted for non swirling flame and fire whirl

Figure 4.12 shows temperature isocontours for sub ($\Gamma^* = 7.40$), natural and supra ($\Gamma^* = 17.82$) aspirated cases. In all cases the maximum temperature is located at the shear layer near the flame origin. The increase in circulation is associated with an increase in the fire whirl centreline temperature. On the "naturally aspirated" case the temperature in the centreline is lower than the flame front temperature, contrary to the case $\Gamma^* = 17.82$, where the centreline is already similar to the flame front. The temperature on the core of flame is higher for larger circulation than the "naturally aspirated" case and it is related with the shortening of the flame.

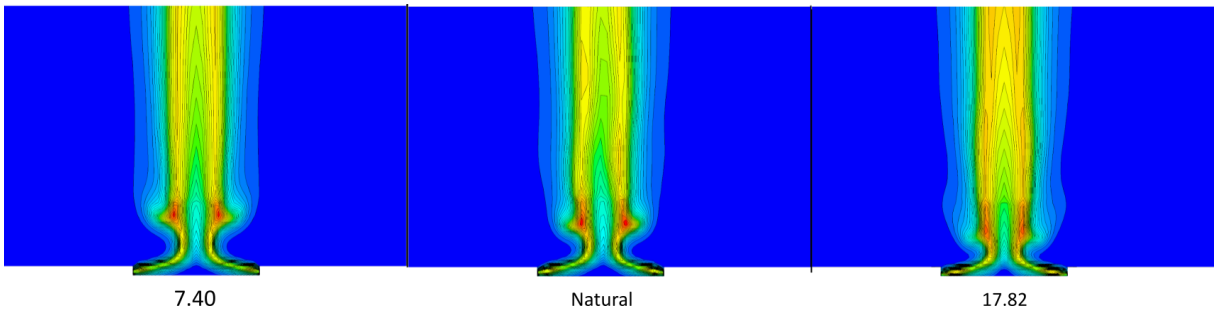


Figure 4.12: Isolines of temperature

### 4.3.3 Turbulence

Figures 4.13 and 4.14 a) show the turbulent kinetic energy contour for a $300$ kW non swirling diffusion flame and $150$ kW respectively, and figures 4.13 and 4.14 b) show the fire whirl case for $300$ kW and $150$ kW respectively. The non swirling flame shows an increase of turbulent kinetic energy with height,

reaching the highest values on the top of the flame. In contrast, the fire whirl presented larger values at the base, due to the gradients induced by the radial inflow layer. On the fire whirl body the values are much lower than in the analogous buoyant flame, suggesting the existence of turbulence suppression. Radial velocity fluctuations on the fire whirl are attenuated due to high centrifugal forces, decreasing turbulence compared with analogous non swirling flows. The decrease in turbulence in fire whirls compared with analogous diffusion flames is in agreement with the observations of Snegirev *et al.* [19]. These decrease of turbulent kinetic energy is associated with a decrease of turbulent mixing of fuel with the entrained air. Consequently the decrease on turbulent mixing requires greater flame surface which is obtained with the increase in flame height as explained by [19]

(a) Non swirling buoyant flame (b) Fire whirl

Figure 4.13: Turbulent kinetic energy for $300$ kW no swirling flame and $300$ kW fire whirl

(a) Non swirling buoyant flame (b) Fire whirl

Figure 4.14: Turbulent kinetic energy for $150$ kW no swirling flame and $150$ kW fire whirl

Figures 4.16 and 4.17 show the variation with height of the Reynolds stress $\overline{v'w'}$ for several circulation ($\Gamma^*$) case studies and the considered heat releases of $150$ and $300$ kW. The highest value of $\overline{v'w'}$ is obtained at the base of the fire whirl, and in general is proportional to circulation. The highest value on the base of fire whirl is associated with the gradients induced by the radial inflows layer. Higher $\Gamma^*$ is associated with an intensification of the radial inflow on the fire whirl base, consequently increasing the shear stress and turbulence parameters.

Along the fire whirl height $\overline{v'w'}$ decreases, suggesting the existence of turbulence suppression. Note

that although the highest circulation $\Gamma^*$ promotes greater $\overline{v'w'}$ production on the fire whirl base, it is also associated with greater decrease along the fire whirl height.

Figure 4.15 shows the isocontours of $\overline{v'w'}$ on the base of the fire whirl. Two peaks of $\overline{v'w'}$ are observed, corresponding to the one present on figure 4.16, 4.17 and 4.18. The existence of these two peaks is related with the flow pattern described before. The streamline curvature induced by the inflow layer and flame expansion results on production of shear stresses. Figure 4.15 shows the isocontour of $\overline{v'w'}$ and velocity vectors of a typical fire whirl, $P = 150$ kW. The location of the maximum production of $\overline{v'w'}$ is coincident with curvature of the streamlines and with the flame expansion zone.

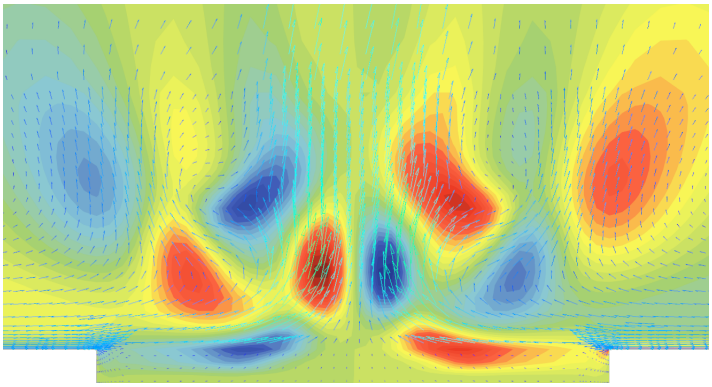

Figure 4.15: Isocontour of $\overline{v'w'}$ and velocity vectors for a typical $150$ kW fire whirl

The $\overline{v'w'}$ profiles compliant with the analyses of the turbulent kinetic energy on the fire whirl figure 4.13b). The flow pattern and the radial inflow on the fire whirl impact on the $\overline{v'w'}$ profiles and production, clarifies the highest values of turbulent kinetic energy on the base of fire whirls.

The evolution of turbulence suppression has been analysed on light of Richardson number, due to the effect of swirl or streamline curvature on turbulent flow which is analogous to buoyancy [46, 53]. In this study we calculate the Richardson number (Ri) proposed by [22] based on the modelling of the ratio of mixing lengths. Figure 4.19 shows the predicted Richardson number along the centreline and the measured data from [22]. High values of Ri suggest turbulence suppression and the high Richardson values are predicted on the fire whirl bottom and they are consistent with experimental data from [22]. One should note that according with the definition of Richardson proposed by [22], the Richardson number along the centreline of a non swirling buoyant flame is always zero, indicating turbulence suppression in not present on an analogous non swirling flame.

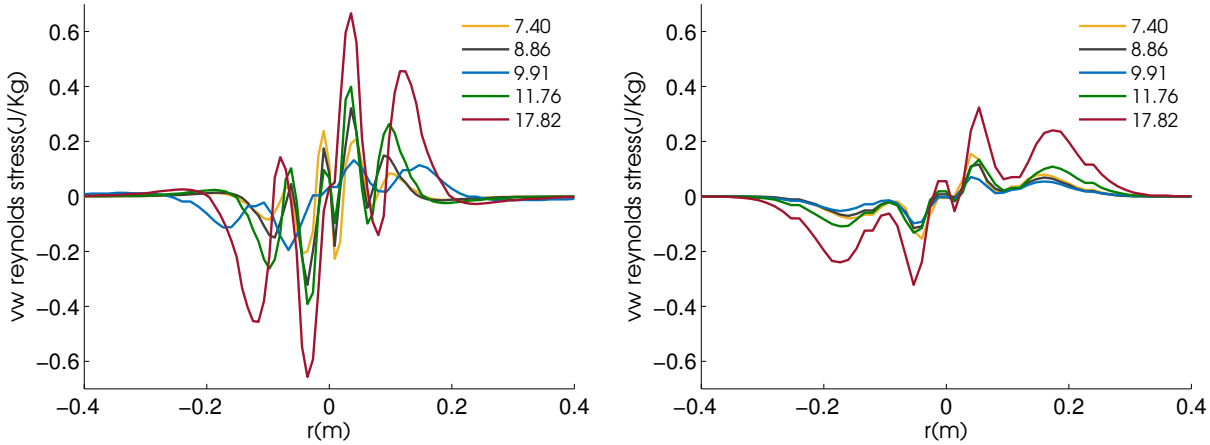


(a) 0.3D (b) 0.7D

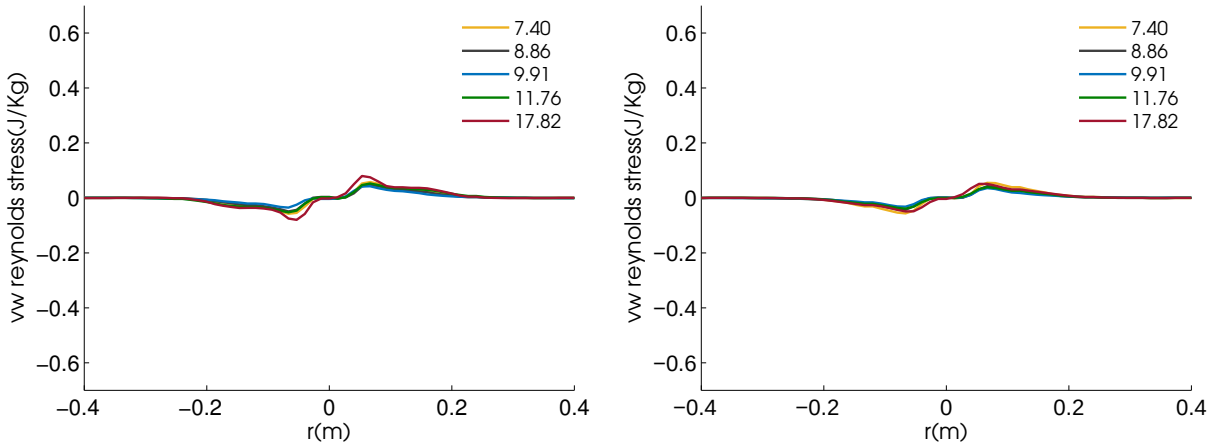


(c) 1.7D (d) 3D

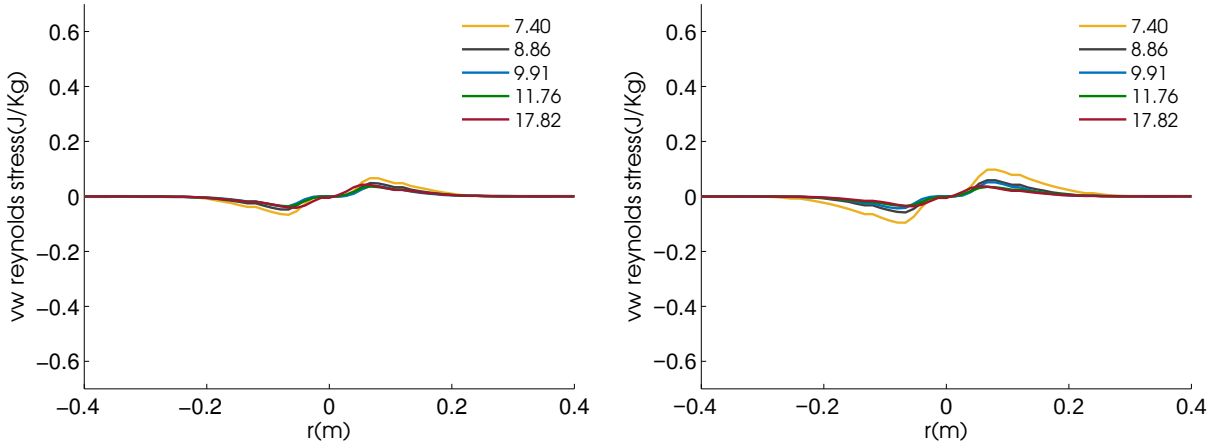


(e) 5D (f) 7D

Figure 4.16: Turbulence profiles for $Q = 150$ kW

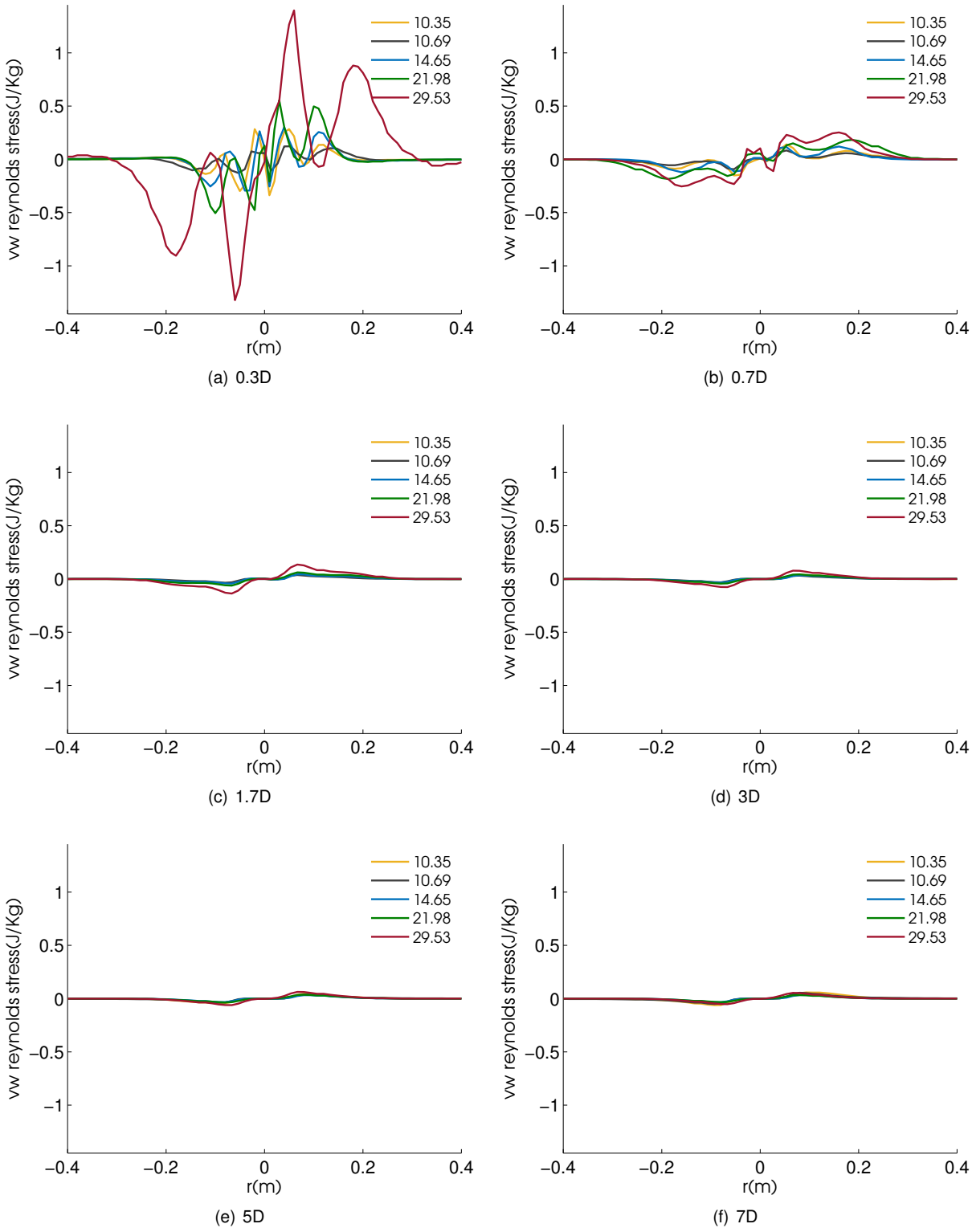


Figure 4.17: Turbulence profiles for $Q = 300$ kW

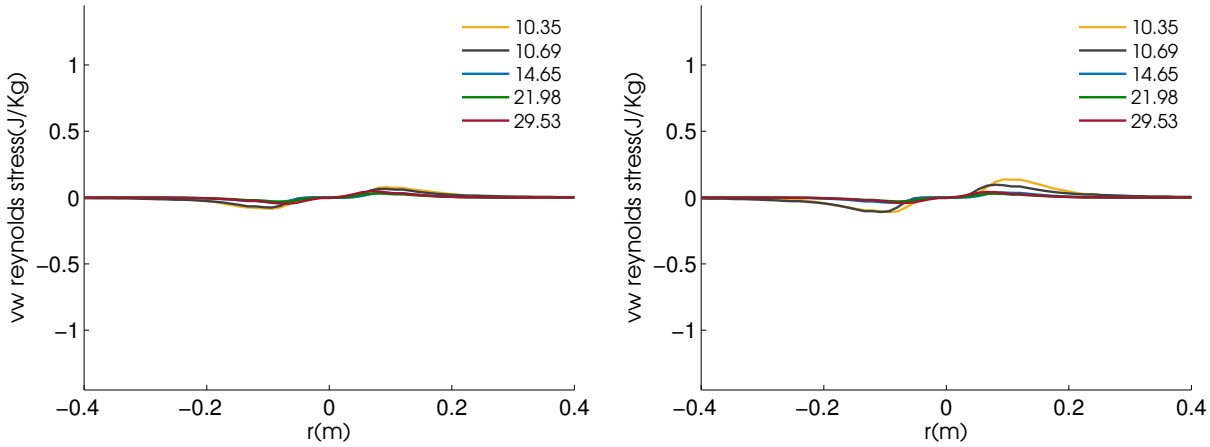


Figure 4.18: Turbulence profiles for $Q = 300$ kW

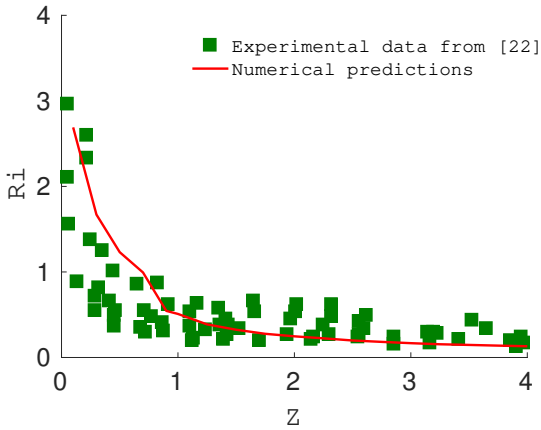


Figure 4.19: Richardson vs height from predictions and experimental data from [22]

# Chapter 5

# Conclusions and Achievements

Numerical simulations of laboratory fire whirls were conducted and analysed. The commercial code Star-CCM+® was used to fulfil the proposed objectives of this dissertation.

The challenges placed on the numerical modelling of fire whirls due to their complexity required a carefully evaluation of key models such as boundary conditions and turbulence models. Three turbulence models, RST, Standard $\kappa - \epsilon$ and LAG EB $\kappa - \epsilon$, were evaluated. The performance of both two equations $\kappa - \epsilon$ models proved to be insufficient, contrary to the RST one, demonstrating the necessity of second order closures for capturing at least some of the complex phenomenon of buoyant and swirling turbulent flows. Consequently, such results dictated the selection of the RST model.

The simulations were validated with available experimental data for a considerable range of fuel mass flow rate supplies ranging from $2$ to $300$ kW.

The boundary conditions used are physically bounded and together with the differential second order turbulence model allow to capture the average features from the base to the top of laboratory fire whirls, proved by the satisfactory agreement between the numerical predictions and the experimental temperature and velocity along the radial and centreline profiles and with flame height.

The obtained good agreement between the radial profile of tangential velocity of fire whirls and the analogous profile from the analytical solutions of a Burgers vortex shows that the fire whirl flow kinematics are well described by the Burgers vortex. The predicted velocity profiles on the floor boundary layer is in agreement with the analytical Ekman solution, indicating that the boundary layer present on the floor is an Ekman type. The analysis of the present boundary layer shows that it has a direct impact on the shape and flow patterns present on the fire whirl base as well as on the fuel consumption for different circulations.

The sensitivity and dependence of circulation on flame height was investigated. For each heat release considered, a critical circulation that maximizes the flame height was found. The circulation for which the flame height is maximum depends on the heat release and it is proportional to the non dimensional heat release. A correlation for the flame height dependence with circulation was deduced in good agreement with available experimental and numerical data.

The turbulence field of a fire whirl was analysed and compared with an analogous non swirling buoyant

flame with the same fuel rate supply. Larger values of the shear stress component $\overline{v'w'}$ were obtained at the fire whirl base. The predicted values are proportional to circulation. Such results suggest the direct impact on shear layer by the inflow layer. The larger values of $\overline{v'w'}$ justifies the obtained turbulent kinetic energy profile on the base of fire whirls. The lower values of turbulent kinetic energy compared with the analogous no swirling buoyant flame suggest the existence of turbulence suppression. The evolution of turbulence suppression along the fire whirl height was analysed in light of Richardson number. The predicted Richardson number is consistent with available experimental data, suggesting a decrease of turbulence suppression along the fire whirl height.

Finally, the results obtained, specially for the validation against available experimental data, highlight the potential of the RST approach to help achieve a better understanding of the fundamental knowledge of the driving mechanism and physical behaviour of fire whirls.

## 5.1 Future work

As future work for the study of the driving mechanism and physical behaviour of fire whirls a detailed study of the fire whirl base should be considered. Moreover the effect of puffing and precession reported on literature should be numerically investigated with a more accurate model such as LES. Finally, the vorticity and fire whirl generation on open configurations should be addressed, and the flame structure should be compared with the ones obtained from laboratory studies.

# Bibliography


[1] R. Dobashi, T. Okura, R. Nagaoka, Y. Hayashi, and T. Mogi. Experimental Study on Flame Height and Radiant Heat of Fire Whirls. *Fire Technology*, 52(4):1069–1080, 2016. ISSN 15728099. doi: 10.1007/s10694-015-0549-z.

[2] J. M. Forthofer and S. L. Goodrick. Review of vortices in wildland fire, 2011. ISSN 20901968.

[3] A. Tohidi, M. J. Gollner, and H. Xiao. Fire Whirls. *Annual Review of Fluid Mechanics*, 50, 2018. ISSN 0066-4189. URL `http://www.annualreviews.org/doi/10.1146/annurev-fluid-122316-045209`.

[4] K. A. Hartl and A. J. Smits. Scaling of a small scale burner fire whirl. *Combustion and Flame*, 2016. ISSN 15562921. doi: 10.1016/j.combustflame.2015.09.027.

[5] K. Kuwana, K. Sekimoto, K. Saito, and W. F. A. Scaling fire whirls. *Fire Safety Journal*, 43(4): 252–257, 2008. ISSN 03797112. doi: 10.1016/j.firesaf.2007.10.006.

[6] J. Lei, N. Liu, L. Zhang, H. Chen, L. Shu, P. Chen, Z. Deng, J. Zhu, K. Satoh, and J. L. De Ris. Experimental research on combustion dynamics of medium-scale fire whirl. *Proceedings of the Combustion Institute*, 2011. ISSN 15407489. doi: 10.1016/j.proci.2010.06.009.

[7] S. Soma and K. Saito. Reconstruction of fire whirls using scale models. *Combustion and Flame*, 1991. ISSN 00102180. doi: 10.1016/0010-2180(91)90107-M.

[8] J. Lei, N. Liu, L. Zhang, Z. Deng, N. K. Akafuah, T. Li, K. Saito, and K. Satoh. Burning rates of liquid fuels in fire whirls. *Combustion and Flame*, 159(6):2104–2114, 2012. ISSN 15562921. doi: 10.1016/j.combustflame.2012.01.019. URL `http://dx.doi.org/10.1016/j.combustflame.2012.01.019`.

[9] H. Xiao, M. J. Gollner, and E. S. Oran. From fire whirls to blue whirls and combustion with reduced pollution. *Proceedings of the National Academy of Sciences*, 2016. ISSN 0027-8424. doi: 10.1073/pnas.1605860113.

[10] S. B. Hariharan, E. T. Sluder, M. J. Gollner, and E. S. Oran. Thermal structure of the blue whirl. *Proceedings of the Combustion Institute*, 2018. ISSN 15407489. doi: 10.1016/j.proci.2018.05.115.

[11] J. Lei, C. Ji, N. Liu, and L. Zhang. Effect of imposed circulation on temperature and velocity in general fire whirl: An experimental investigation. *Proceedings of the Combustion Institute*, 000:

1–8, 2018. ISSN 15407489. doi: 10.1016/j.proci.2018.06.055. URL https://doi.org/10.1016/j.proci.2018.06.055.

[12] C. Pinto, D. Viegas, M. Almeida, and J. Raposo. Fire whirls in forest fires: An experimental analysis. *Fire Safety Journal*, 87(November 2016):37–48, 2017. ISSN 03797112. doi: 10.1016/j.firesaf.2016.11.004. URL http://dx.doi.org/10.1016/j.firesaf.2016.11.004.

[13] J. Lei, N. Liu, and K. Satoh. Buoyant pool fires under imposed circulations before the formation of fire whirls. *Proceedings of the Combustion Institute*, 2015. ISSN 15407489. doi: 10.1016/j.proci.2014.05.110.

[14] N. Liu, Q. Liu, Z. Deng, S. Kohyu, and J. Zhu. Burn-out time data analysis on interaction effects among multiple fires in fire arrays. *Proceedings of the Combustion Institute*, 2007. ISSN 15407489. doi: 10.1016/j.proci.2006.08.110.

[15] P. B. Dermer, A. Y. Varaksin, and A. I. Leontiev. The wall-free non-stationary fire whirls generation by axisymmetric burning of solid fuel pellets. *International Journal of Heat and Mass Transfer*, 110:890–897, 2017. ISSN 00179310. doi: 10.1016/j.ijheatmasstransfer.2017.03.076. URL http://dx.doi.org/10.1016/j.ijheatmasstransfer.2017.03.076.

[16] R. Zhou and Z. N. Wu. Fire whirls due to surrounding flame sources and the influence of the rotation speed on the flame height. *Journal of Fluid Mechanics*, 2007. ISSN 00221120. doi: 10.1017/S0022112007006337.

[17] H. Yu, S. Guo, M. Peng, Q. Li, J. Ruan, W. Wan, and C. Chen. Study on the influence of air-inlet width on fire whirls combustion characteristic. In *Procedia Engineering*, 2013. doi: 10.1016/j.proeng.2013.08.130.

[18] F. Battaglia, K. B. McGrattan, R. G. Rehm, and H. R. Baum. Simulating fire whirls. *Combustion Theory and Modelling*, 2000. ISSN 13647830. doi: 10.1088/1364-7830/4/2/303.

[19] A. Snegirev, J. Marsden, J. Francis, and G. Makhviladze. Numerical studies and experimental observations of whirling flames. *International Journal of Heat and Mass Transfer*, 2004. ISSN 00179310. doi: 10.1016/j.ijheatmasstransfer.2004.02.002.

[20] J. Lei, N. Liu, Y. Jiao, and S. Zhang. Experimental investigation on flame patterns of buoyant diffusion flame in a large range of imposed circulations. *Proceedings of the Combustion Institute*, 36(2):3149–3156, 2017. ISSN 15407489. doi: 10.1016/j.proci.2016.06.072. URL http://dx.doi.org/10.1016/j.proci.2016.06.072.

[21] K. Zhou, N. Liu, J. S. Lozano, Y. Shan, B. Yao, and K. Satoh. Effect of flow circulation on combustion dynamics of fire whirl. *Proceedings of the Combustion Institute*, 34(2):2617–2624, 2013. ISSN 15407489. doi: 10.1016/j.proci.2012.06.053. URL http://dx.doi.org/10.1016/j.proci.2012.06.053.

[22] J. Lei, N. Liu, and R. Tu. Flame height of turbulent fire whirls: A model study by concept of turbulence suppression. *Proceedings of the Combustion Institute*, 2017. ISSN 15407489. doi: 10.1016/j.proci.2016.06.080.

[23] W. K. Chow and S. S. Han. Experimental Data on Scale Modeling Studies on Internal Fire Whirls. 10(3):63–74, 2011.

[24] J. Lei, N. Liu, and K. Satoh. Buoyant pool fires under imposed circulations before the formation of fire whirls. *Proceedings of the Combustion Institute*, 2015. ISSN 15407489. doi: 10.1016/j.proci.2014.05.110.

[25] J. Lei, N. Liu, J. S. Lozano, L. Zhang, Z. Deng, and K. Satoh. Experimental research on flame revolution and precession of fire whirls. *Proceedings of the Combustion Institute*, 2013. ISSN 15407489. doi: 10.1016/j.proci.2012.06.126.

[26] J. Lei and N. Liu. Flame precession of fire whirls: A further experimental study. *Fire Safety Journal*, 79:1–9, 2016. ISSN 03797112. doi: 10.1016/j.firesaf.2015.10.005. URL `http://dx.doi.org/10.1016/j.firesaf.2015.10.005`.

[27] P. Wang, N. Liu, L. Zhang, Y. Bai, and K. Satoh. Fire Whirl Experimental Facility with No Enclosure of Solid Walls: Design and Validation. *Fire Technology*, 2015. ISSN 15728099. doi: 10.1007/s10694-014-0435-0.

[28] D. Yu and P. Zhang. On the flame height of circulation-controlled firewhirls with variable density. *Proceedings of the Combustion Institute*, 2015. ISSN 15407489. doi: 10.1016/j.proci.2016.06.063.

[29] D. Yu and P. Zhang. On flame height of circulation-controlled firewhirls with variable physical properties and in power-law vortices: A mass-diffusivity-ratio model correction. *Combustion and Flame*, 2017. ISSN 15562921. doi: 10.1016/j.combustflame.2017.04.008.

[30] D. Yu and P. Zhang. Circulation-controlled firewhirls with differential diffusion. *Combustion and Flame*, 2018. ISSN 15562921. doi: 10.1016/j.combustflame.2017.10.040.

[31] A. Y. Klimenko and F. A. Williams. On the flame length in firewhirls with strong vorticity. *Combustion and Flame*, 2013. ISSN 00102180. doi: 10.1016/j.combustflame.2012.10.019.

[32] H. W. Emmons and S.-J. Ying. The fire whirl. *Symposium (International) on Combustion*, 1967. ISSN 00820784. doi: 10.1016/S0082-0784(67)80172-3.

[33] A. C. Yuen, G. H. Yeoh, S. C. Cheung, Q. N. Chan, T. B. Chen, W. Yang, and H. Lu. Numerical study of the development and angular speed of a small-scale fire whirl. *Journal of Computational Science*, 2018. ISSN 18777503. doi: 10.1016/j.jocs.2018.04.021.

[34] G. W. Zou and W. K. Chow. Generation of an internal fire whirl in an open roof vertical shaft model with a single corner gap. *Journal of Fire Sciences*, 2015. ISSN 15308049. doi: 10.1177/0734904115569703.

[35] K. Hanjalić. One-Point Closure Models for Buoyancy-Driven Turbulent Flows. *Annual Review of Fluid Mechanics*, 2002. ISSN 0066-4189. doi: 10.1146/annurev.fluid.34.082801.161035.

[36] J. C. F. Pereira and J. M. P. Rocha. Simulation of shear orientation effects on stably stratified homogeneous turbulence with RANS second-order modelling. *Journal of Turbulence*, 10(43):1–35, 2009. ISSN 14685248. doi: 10.1080/14685240903314602.

[37] J. C. F. Pereira and J. M. P. Rocha. Prediction of stably stratified homogeneous shear flows with second-order turbulence models. *Fluid Dynamics Research*, 42(4):45509, 2010. ISSN 0169-5983. doi: 0.1088/0169-5983/42/4/045509. URL `http://stacks.iop.org/1873-7005/42/i=4/a=045509`.

[38] W. K. Chow, J. F. Dang, Y. Gao, and C. L. Chow. Dependence of flame height of internal fire whirl in a vertical shaft on fuel burning rate in pool fire. *Applied Thermal Engineering*, 121:712–720, 2017. ISSN 13594311. doi: 10.1016/j.applthermaleng.2017.04.108. URL `http://dx.doi.org/10.1016/j.applthermaleng.2017.04.108`.

[39] F. White. *Fluid mechanics*. McGraw-Hill, 7th edition, 2010.

[40] H. K. Versteeg and W. Malalasekera. *An Introduction to computational fluid Dynamics*. Pearson Education, 2nd edition, 2007.

[41] P. Davidson. *Turbulence An introduction for Scientists and Engineers*. Oxford University Press, 1st edition, 2004.

[42] V. Brederode. *Aerodinâmica Incompressível: Fundamentos*. IST Press, 2nd edition, 2018.

[43] J. O. Hinze. *Turbulence*. McGraw-Hill, 1975.

[44] D. B. Spalding. Mixing and chemical reaction in steady confined turbulent flames. *Symposium (International) on Combustion*, 1971. ISSN 00820784. doi: 10.1016/S0082-0784(71)80067-X.

[45] B. F. Magnussen and B. H. Hjertager. On mathematical modeling of turbulent combustion with special emphasis on soot formation and combustion. *Symposium (International) on Combustion*, 1977. ISSN 00820784. doi: 10.1016/S0082-0784(77)80366-4.

[46] D. G. Lilley. Prediction of Inert Turbulent Swirl Flows. *AIAA Journal*, 11(7):955–960, 1973. ISSN 00011452. doi: doi:10.2514/6.1972-699.

[47] STAR-CCM+ 12.02 documentation.

[48] S. V. Patankar and D. B. Spalding. A calculation procedure for heat, mass and momentum transfer in three-dimensional parabolic flows. *International Journal of Heat and Mass Transfer*, 1972. ISSN 00179310. doi: 10.1016/0017-9310(72)90054-3.

[49] S. V. Patankar. A calculation procedure for two-dimensional elliptic situations. *Numerical Heat Transfer*, 1981. ISSN 01495720. doi: 10.1080/01495728108961801.

[50] F. Moukalled, L. Mangani, and M. Darwish. *The Finite Volume Method in Computational Fluid Dynamics*. Springer, 2016.

[51] Guide for the Verification and Validation of Computacional Fluid Dynamics Simulations, 2002.

[52] J. Lei, N. Liu, L. Zhang, and K. Satoh. Temperature, velocity and air entrainment of fire whirl plume: A comprehensive experimental investigation. *Combustion and Flame*, 162(3):745–758, 2015. ISSN 15562921. doi: 10.1016/j.combustflame.2014.08.017. URL `http://dx.doi.org/10.1016/j.combustflame.2014.08.017`.

[53] J. M. Beér, N. A. Chigier, T. W. Davies, and K. Bassindale. Laminarization of turbulent flames in rotating environments. *Combustion and Flame*, 1971. ISSN 00102180. doi: 10.1016/S0010-2180(71)80009-3.